Journal of Materials Chemistry A

ROYAL SOCIETY OF CHEMISTRY

REVIEW

View Article Online
View Journal | View Issue

Cite this: J. Mater. Chem. A, 2025, 13, 28819

Advances, challenges, and perspectives in developing $CuInX_2$ (X = S, Se) nanomaterials for solar energy conversion applications

L. Páramo,[ab] M. Pains Duarte,[ab] G. Fuoco,[ab] A. Adedapo,[ab] D. P. Singh [c] and R. Naccache *[ab]

Received 27th June 2025
Accepted 4th August 2025

DOI: 10.1039/d5ta05229g

rsc.li/materials-a

$CuInX_2$ (where X = S, Se) are among group I–III–VI's most recognized semiconductors in the ternary chalcogenides. These materials have come to the forefront of solar energy research owing to their optical and electronic properties, such as high absorption coefficients, tunable band gaps, and excellent thermal stability. This positions them as sustainable and low-cost alternatives for solar energy conversion devices. However, their practical implementation remains hindered due to several challenges, including low efficiencies associated with insufficient control in defect formation, variable stoichiometries, ligand selection, and binary or ternary compositional mixtures. A particularly limiting barrier is the current lack of understanding of the emission processes in these materials. Bringing these materials to light and their implementation in fabricating energy conversion devices will crystallize through overcoming these challenges. This review critically examines recent advances in the synthesis, characterization, and integration of $CuInX_2$ systems in solar energy-converting devices, highlighting current challenges and opportunities and offering insights that will not only accelerate research in this field but also contribute to the advancement of other ternary or quaternary copper-based chalcogenides.

1. Introduction

The rise in global energy demands owing to population growth and industrial development, combined with the heavy reliance on fossil fuels, has highlighted the need for a shift toward renewable energy.[1] Fossil fuels, which still account for about 80% of global energy consumption, are non-renewable sources and major contributors to climate change.[2] According to the Energy Institute (EI) report, in 2023, the combustion of fossil fuels contributed to 87% of total CO_2 emissions.[3] Thus, searching for renewable sources and clean energies that meet global energy requirements has become crucial to preserving the environment and promoting a sustainable future. The International Energy Agency (IEA) expects sectors such as transportation, power, and heat to increase their consumption of about 60% of renewable energies in 2030, leading to a 20% share of the total energy consumption.[4]

Solar energy has emerged as one of the most promising renewable alternatives due to its abundance, inexhaustibility, and environmentally friendly features. The sun provides an amount of energy of ~170 000 TWh.[5,6] At the same time, according to IEA, in 2023, the global electricity demand was 26 000 TWh per year,[2] which supports the idea that the sun can meet global energy demand. As such, photovoltaics (PV), which convert sunlight directly into electricity, have emerged as a key solution to use this widely available energy[7] PV cells can be classified into three significant generations: (i) mono- or multi-crystalline silicon, which is the dominant technology utilized globally, (ii) thin-film cells, which includes amorphous silicon, cadmium telluride (CdTe), cadmium sulfide (CdS), as well as copper indium gallium selenide (CIGS) cells, and (iii) the emerging technologies, which includes dye-sensitized, organic, perovskite and quantum dots (QDs) solar cells.[6–9] According to the Renewables 2024 report by the IEA,[4] PV cells are expected to contribute to 80% of the global expansion of the renewable energy share, making solar power the largest renewable energy source. Although silicon-based solar cells currently dominate the market, they face several limitations related mainly to material and processing cost.[7,9] The second and third PV cell generations were developed to reduce costs in this context. Although the second generation showed cost-effectiveness compared to the silicon counterparts, it presented some drawbacks related mainly to low efficiency and toxicity, which hindered large scale applications. Thus, the third generation emerged to overcome production costs and materials inefficiency. These solar cells have attracted significant attention due

[a]Department of Chemistry and Biochemistry and the Centre for NanoScience Research, Concordia University, Montreal, Quebec H3G 1M8, Canada. E-mail: rafik.naccache@concordia.ca

[b]Quebec Centre for Advanced Materials, Concordia University, Montreal, Quebec H3G 1M8, Canada

[c]Université du Littoral Côte d'Opale, UR 4476, UDSMM, Unité de Dynamique et Structure des Matériaux Moléculaires, F-62228 Calais, France

to their high efficiency, lower costs, and excellent material flexibility.[8,11,12] Among them, QD solar cells stand out owing to their unique optical and electronic properties, such as size-tunable bandgap, endowing them with a broader absorption range of the solar spectrum.[12–14] Nonetheless, one of the challenges QD-based cells face is their reliance on toxic metals, as the most commonly used QDs comprise Cd and Pb and include CdS, CdTe, PbS, and PbSe.[14,15] In an attempt to address these shortcomings, recent research has focused on the design of more sustainable and greener QDs with solar cells based on ternary chalcogenides, with $CuInX_2$ nanocrystals becoming a popular alternative.[16,17] This is not only due to the fact that $CuInX_2$ nanomaterials possess appropriate optical and electronic properties, but also their constituent elements are considered to be non-toxic to human health and the environment. Moreover, copper, sulfur, and selenium are relatively abundant. In contrast, while indium is regarded as a scarce material compared to the others, its environmental impact remains low.[18–20]

$CuInS_2$ and $CuInSe_2$ nanomaterials have been among the most explored compounds for solar energy in the I–III–VI_2 ternary chalcopyrite semiconductors group, which belongs to the broad family of Cu-chalcogenides.[18] These compounds exhibit a chalcopyrite crystalline structure, where the atoms Cu, In, S, and/or Se are arranged tetrahedrally. They also have an abundance of intrinsic defects, which guarantee them diverse optoelectronic properties.[21,22] These compounds have been widely investigated for use in QDs-solar cells due to their unique optoelectronic properties, such as high energy conversion, significant Stokes shifts, tunable band gaps, and high absorption coefficients.[13,18–20,22] The ability to tune their direct bandgaps based on the size or elemental composition renders them efficient sunlight absorbers across a broad spectrum of wavelengths, from the visible to near-infrared (NIR).[15,18,23] The band gap of $CuInS_2$ is ~1.5 eV, which matches the solar irradiance spectrum peak. $CuInSe_2$ has a smaller bandgap of ~1.04 eV, so it absorbs more infrared light. In this context, these materials have proven to be appropriate for photovoltaic applications.[20,24,25]

Furthermore, $CuInX_2$ materials offer an essential advantage relative to traditional materials used in other PV cells, such as silicon, given their high absorption coefficients often exceeding 10^5 cm^{-1}.[19,24] This enables them to efficiently absorb sunlight in layers typically less than several micrometers thick, compared to the 100 mm layers required in silicon-based PVs.[18] As a result, $CuInX_2$ solar cells reduce material usage and production costs, making them a promising option for PV cell technology.[8] Given their aforementioned advantages, $CuInX_2$ nanomaterials have not only been applied in solar cells but also explored in biomedicine,[26] tandem devices,[27] photocatalysis,[28] LEDs,[29] and luminescent solar concentrators (LSC).[30] LSCs have proven to be one of the most significant devices developed in the field. LSCs can be incorporated or doped with different photoluminescent materials, such as organic dyes and QDs, to enhance their properties. Organic dyes were initially used, but their application was limited owing to narrow absorption bands and significant reabsorption losses. On the other hand, QDs offer advantages over organic dyes, such as a larger Stokes shift, broader absorption spectra, and improved power conversion efficiency (PCE), providing a simple and low-cost alternative to converting sunlight into electricity.[31,32]

Despite their attractive and promising features, applying these nanomaterials in QD solar cells still faces several challenges. Recent research has been focused on addressing these issues to improve performance and efficiency. One major challenge is the incomplete understanding of their emission mechanisms, which hinders the development of materials with enhanced properties, such as high quantum yields (QY).[24,33,34] Another challenge is associated with the synthesis, including the selection of suitable ligands, which play a crucial role in charge transfer efficiency,[15,18] and the insertion of selenium into the structure due to the limited availability of Se precursors compared to sulfur.[35] Additionally, strategies to improve the PCE of QD-based solar cells have been explored, with recent studies focusing on grain boundaries, which can enhance charge transfer and consequently enhance device performance.[18]

Thus, this review aims to provide a comprehensive overview of recent design and application strategies for $CuInX_2$ nanomaterials for solar energy conversion. The review also explores the fundamental properties of $CuInX_2$ materials, focusing on their structure, optical and electrical properties, recent progress, research gaps in the synthesis of these materials, their emission processes, and their role in solar energy conversion devices such as PV cells and LSCs.

2. Fundamental properties of $CuInX_2$ nanomaterials

2.1. Structural characteristics

$CuInS_2$ and $CuInSe_2$ represent one of the most popular I–III–IV compositions of the ternary copper chalcogenide family; both materials have received special attention for applications in light-emitting devices, solar absorbers, and devices for solar energy conversion.[31,36,37] Both materials share structural similarities in their available crystalline phases, with the main difference being the anion difference, which affects their optoelectronic properties. This change in anion size dramatically affects properties like photoluminescence (PL), where most reported $CuInS_2$ emission is in the red region. In contrast, $CuInSe_2$ emission is primarily located in the near-infrared.[38–40]

In $CuInX_2$ (X = S, Se), copper exists in the +1 oxidation state, indium in the +3 oxidation state, while S or Se are in the −2 oxidation state.[41] In terms of crystalline structure, $CuInX_2$ (X = S, Se) can exist in three phases, namely chalcopyrite,[42–47] zinc blend,[48–50] and wurtzite.[41,50] Among these, chalcopyrite is the most reported in nanomaterials synthesis due to its low energy of formation and high stability.[36,39,41,42,51] The chalcopyrite unit cell structure can be constructed from the traditional zinc blend structure in ZnS by the alternate substitution of Zn sites with In and Cu cations; the differences in bond lengths between Cu and In cause a distortion in the unit cell, leading to a tetragonal unit cell, on the other hand $CuInS_2$ and $CuInSe_2$ in zinc blende

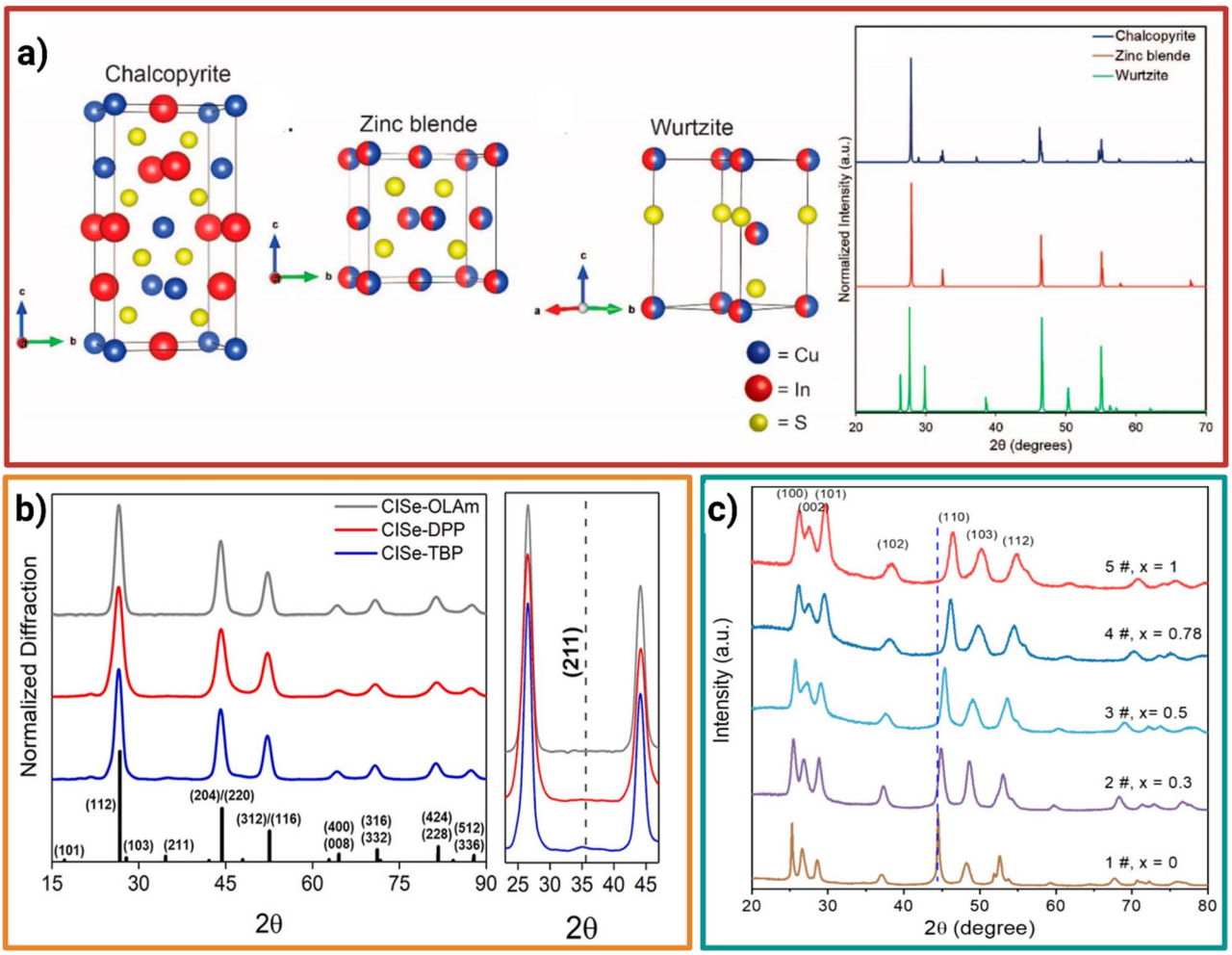

Fig. 1 (a) Unit cells of chalcopyrite, zinc blende, wurtzite, and simulated XRD spectra of the three $CuInS_2$ crystalline phases, adapted with permission from ref. 19. Copyright 2016 American Chemical Society. (b) XRD diffractogram of chalcopyrite $CuInSe_2$ synthesized with different surface ligands, adapted with permission from ref. 40. Copyright 2021 American Chemical Society. (c) XRD diffractogram of wurtzite $CuIn(S_x/Se_{1-x})_2$ with different compositions of S/Se, adapted with permission from ref. 37. Copyright 2024 American Chemical Society.

phase possess an structure in which the Cu and In atoms are randomly organized within the structure leading to a cationic disorder within a cubic lattice.[18] Unit cells of the chalcopyrite, zinc blende, and wurtzite can be seen in Fig. 1a. The distinction between the chalcopyrite phase and $CuInX_2$ zinc blende can be challenging since both phases share a Bragg reflection of high intensity at similar angles,[19] as seen in Fig. 1a. The distinction between the two phases commonly relies on the lowest intensity reflections, although signal broadening opacifies the low-intensity reflections in nanomaterials.[19] Studies have shown that the use of different ligands can lead to materials with similar crystallographic characteristics, as demonstrated by Harvey *et al.*[44] where the use of ligands like oleylamine (OLA), diphenylphosphine, and tributyl phosphine yielded nanomaterials in the chalcopyrite phase[44] (Fig. 1b). On the other hand, the wurtzite structure exhibits Bragg reflections located at angles that can be clearly distinguished from the other two crystalline structures.[41] A change in anions from S to Se in the crystal structure can be observed as a shift of the Bragg reflections associated with an increase in the lattice parameter due to the incorporation of a larger ion,[41] as seen in Fig. 1c.

$CuInS_2$ and $CuInSe_2$ are semiconductors with structures rich in various types of defects, which are associated with their optical properties, such as PL. These properties have led to the materials being commonly described as defect-tolerant.[52] Although it is recognized that defects guide the emission processes, the scientific community has not yet reached a consensus on the exact origins of these mechanisms.[19] The existence of multiple stoichiometric ratios is closely related to the formation of defects such as copper vacancies and indium antisite pairs ($2v_{Cu^-} + In_{Cu^{2+}}$).[46]

2.2. The impact of variable stoichiometries on properties

Depending on the stoichiometry of the ternary composition, one can achieve different opto-electronic properties by simply modifying the content of Cu:In, or even S:Se if binary chalcogen mixtures are used.[41,53] Stoichiometric variation can alter the semiconductor behaviour to p- or n-type, although the p-type is

easier to produce due to the tendency of $CuInX_2$ to be Cu deficient.[18] In wurtzite-type CuIn(S, Se)$_2$, an increase of the S content in the S/Se binary composition translates to an increase in the bandgap value.[41]

Composition is also affected by the choice of ligand, which depends on their chemical properties, as well as their reactivities with metal and chalcogen precursors. Commonly, the hard and soft acid–base (HSAB) theory has been used as a guiding tool to control the reactivity of selected precursors.[44] A comparison between three ligands, tributyl phosphine (TBP), diphenylphosphine (DPP), and OLA, shows that among the three, TBP promoted and increased indium content in the samples compared to OLA and DPP, where the Cu : In ratio was higher.[44] The synthesis temperature also had a profound effect on composition, as demonstrated by Houck *et al.*[46] where samples of $CuInSe_2$ synthesized at 180 °C were copper deficient (Cu : In = 0.52). The Cu : In ratio increased with temperature, yielding a value of 0.72 at 210 °C and reaching 0.92 at 240 °C.[46]

2.3. Optical properties

$CuInS_2$ and $CuInSe_2$ share a similar absorption spectrum, generally characterized as "featureless" with no excitonic peak observed. This is attributed to many different phenomena, including a broad size distribution of the particles or a non-uniform chemical composition.[54] Commonly reported band gap values for $CuInS_2$ range from 1.53 (bulk)[19,55] and 1.04 eV for $CuInSe_2$,[18] while binary mixtures of S/Se vary from 1.21–1.58 eV.[41] In the QD range, properties like the absorption coefficient are affected by particle size[56] as seen in Fig. 2a. Moreover, as previously mentioned, compositional changes lead to the observed differences in absorption and emission processes. For example, an increase in QY has been achieved by reducing the Cu/In ratio. The emission maxima also depends on the Cu/In ratio: a ratio of 1/8 gives an emission centered around 600 nm, while a ratio of 1/4 shifts the emission to around 760 nm.[54] In binary chalcogenides CuIn(S, Se)$_2$, the modification of the S/Se ratio causes a blueshift in the absorption spectra when more sulfur is incorporated into the structure. This blueshift is also accompanied by a change in the bandgap value, with all samples demonstrating p-type semiconductor behavior.[41] It has also been demonstrated that the increase of sulphur concentration in binary chalcogen mixtures leads to an increase in the band gap, as seen in Fig. 2b, where a schematic of band positions is shown based on chalcogen concentration.[41]

Due to their tunable stoichiometry, researchers can manipulate the ratios of reagents such as Cu, In, and S/Se to obtain mixed ternary compositions. Variations in the Cu : In ratio in $CuInSe_2$ influence their optical and crystalline properties. A higher indium-to-copper ratio results in materials with less crystalline structures and fewer defects compared to copper-rich compositions, which are associated with a more ordered crystalline structure.[54] In a study by Guoshuai Wang, $CuInS_2$ with different Cu:In compositions was synthesized. It was observed that an increasing concentration of indium caused a blue shift in the PL spectra along with an increase in PL intensity[52] (Fig. 2c). Similarly, Chen *et al.*[57] reported an increase in PL intensity with higher indium content in copper-deficient $CuInSe_2$; however, at high indium concentrations, while the PL spectra did not exhibit further shifts, the PL intensity decreased[57] (Fig. 2c). Emission spectra can also be redshifted by the increase of the QD size as seen in Fig. 2d, which also results in a redshift of the absorption spectrum.[58]

Another critical factor influencing the opto-electronic properties is the selection of ligands used during the synthesis of $CuInSe_2$.[44] Ligand selection can lead to the formation of either hydrophilic or hydrophobic materials, with hydrophobic materials being the most extensively studied. High-boiling-point solvents, such as octadecene, OLA, and oleic acid (OA), are well-established for the synthesis of colloidal nanomaterials and QDs *via* hot injection methods.[44] Early studies on the formation of nanomaterials, such as $CuInS_2$ and $CuInSe_2$, relied on phosphine ligands, enabling the synthesis of various structures with a wide range of tunable properties. However, in recent years, efforts to develop sustainable synthetic routes using less toxic reagents have led to a reduction in the use of phosphine ligands in favour of alternative surfactants, such as OLA and OA.[59–65] Among these ligands, dodecanethiol (DDT) stands out as a versatile, high-boiling-point solvent that plays multiple roles during the synthesis process. DDT serves as the primary solvent, stabilizing agent, and sulfur source for synthesizing binary, ternary, and quaternary compositions. Its utility has also been extended to the synthesis of $CuInSe_2$, although the incorporation of selenium creates unique challenges that will be addressed in the synthetic routes section (*vide infra*).[38,66–71] Studies have shown that using different ligands, such as tributylphosphine, OLA, and diphenylphosphine, yields $CuInS_2$ materials with varying emission characteristics.[44] While the emission wavelengths remain similar due to comparable particle sizes, QY values differ significantly. For example, $CuInS_2$ QDs capped with OLA exhibited the lowest QY (0.003%), while those synthesized with tributylphosphine achieved the highest values (1.2%).[44] This variation in QY is typically attributed to the ligands' ability to control the defect formation and passivate surface sites, which influence non-radiative emission pathways.[44]

3. Emission processes and current knowledge gaps

Defects in $CuInX_2$ nanocrystals are widely recognized as the primary causes of radiative and non-radiative decay pathways. However, the exact mechanism of PL remains a topic of debate.[19] Recently, studies have firmly attributed the emission processes to free-to-bound mechanisms involving a copper-related trap in either the Cu^+ or Cu^{2+} oxidation states.[72]

In a research article published in 2016, Leach and Macdonald[19] discussed several works to explain the $CuInS_2$ emission processes. In this work, various mechanisms were attributed to the observed photoluminescence (PL), including transitions from the conduction band (CB) to a localized state in the bandgap (BG), donor–acceptor mechanisms, transitions between a localized state and the valence band (VB), as well as

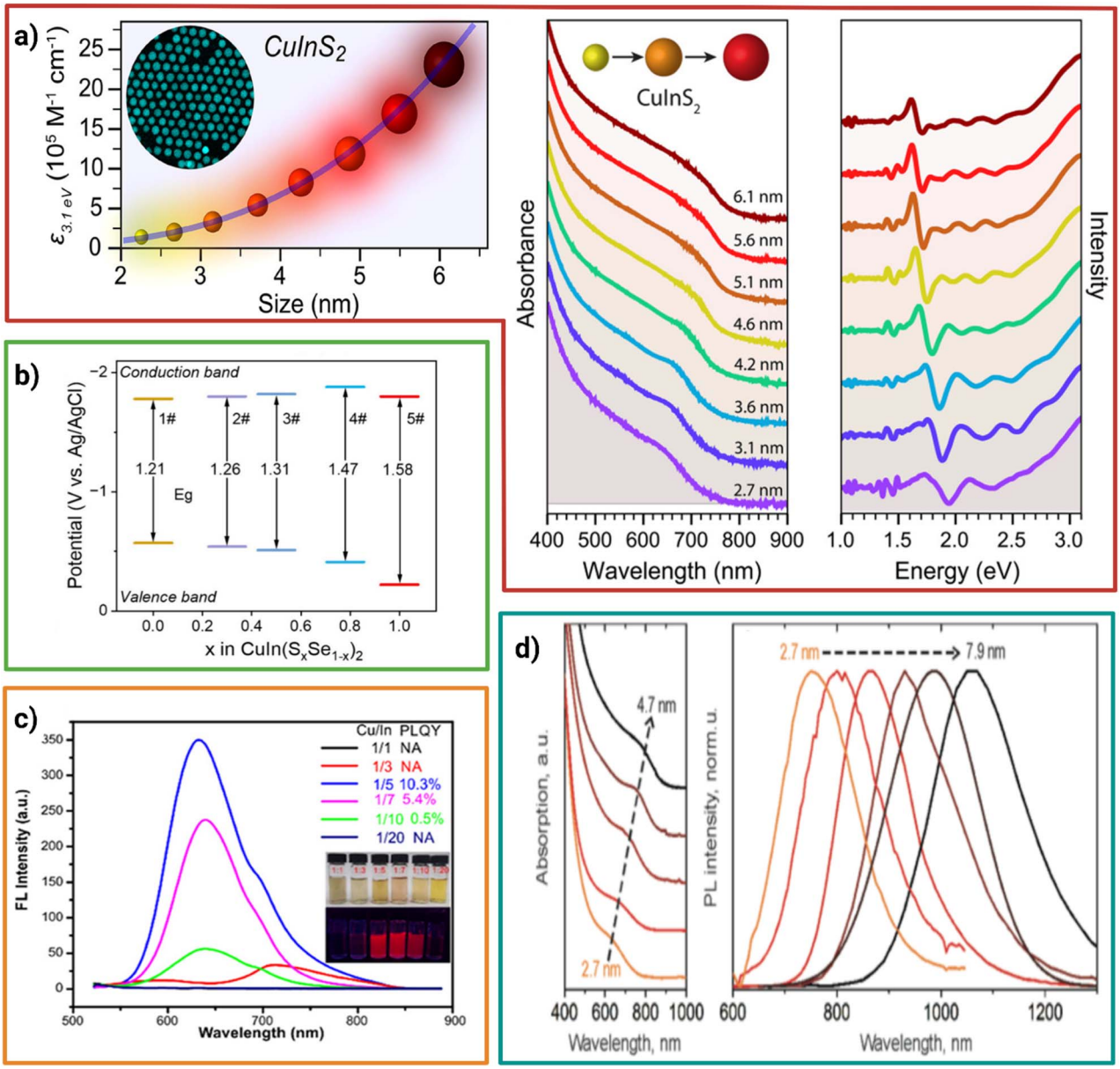

Fig. 2 (a) Size dependence of molar absorption coefficient and absorption spectra of C QDs. Adapted with permission from ref. 54. Copyright 2018 American Chemical Society. (b) Band positions on $CuInS_xSe_{1-x}$ based on chalcogen composition, adapted with permission from ref. 37. Copyright 2024 American Chemical Society, (c) emission spectra of $CuInSe_2$ QDs with varying ratio of Cu/In adapted with permission from ref. 55. Copyright 2012 American Chemical Society. (d) Absorption and emission spectra of $CuInSe_2$ with varying sizes, adapted with permission from ref. 56. Copyright 2013 American Chemical Society.

the presence of Cu^{2+} impurities.[19] The same year, Berends *et al.*[73] analyzed $CuInS_2$ nanocrystals and their counterparts shelled with ZnS and CdS. An analysis of CdS-shelled nanocrystals using time-resolved (TAPL) analysis yielded a negative signal observed at ~530 nm, which was attributed to band-edge bleaching. The authors stated that a donor-to-acceptor type of mechanism requires two trap charges; thus, a band-edge bleach signal shouldn't be observed, ruling this mechanism out.[73] Instead, recombination was associated with a Cu trap, where the radiative decay arises from recombining a delocalized electron to a Cu-related trap. The non-radiative decay pathway was associated with an electron trapping at the material's surface, which, upon shelling, is eliminated, thus increasing PL intensity and lifetime.[73]

Subsequently, Fuhr *et al.*[33] identified reduction and oxidation signals in $CuInS_2$ samples at 350 meV above the VB, which were attributed to the Cu^{1+} and Cu^{2+} oxidation states. In their work, both oxidation states were reported to be PL active, although their distribution depends on the copper content in the samples. Copper-deficient samples were enriched in Cu^{2+} due to charge compensation arising from an increased concentration of copper vacancies. In their proposed mechanism, Cu^{2+} PL involves the recombination of a CB electron with a pre-existing hole in the Cu^{2+} as it has an incomplete 3d shell

([Ar]3d^9). Furthermore, the authors argued that the removal of the photogenerated hole from the VB must occur *via* an existing trap, such as a V_{Cu}, for this pathway to become dominant, as recombination persists for hundreds of nanoseconds. Upon recombination, the reduced Cu^{2+} to Cu^+ requires capturing the hole trapped by the V_{Cu} to recover its +2 state. On the other hand, the mechanisms involving Cu^+ centers involve a capture of a hole to oxidize the Cu^+ to Cu^{2+}, which recombines with the CB electron to form the Cu^+ species.[33] A schematic of the recombination process is shown in Fig. 3a.

In a work published by Nelson and Gamelin,[74] a deep DFT density of states (DOS) analysis of several ZnS structures with different concentrations of Cu^+ and In^{3+} indicated that the VB states acquire a small contribution of the Cu 3d orbital by the single addition of one Cu cation into the structure, which increases as the amount of copper is increased in the structure. On the other hand, the In contribution of the DOS at the CB was not accompanied by a drastic change as compared to copper. As the concentration gradually increased, the VB energy decreased. HOMO analysis of the simulated structure revealed a high contribution of Cu in structures simulated with just one copper atom, as seen in Fig. 3b. Further increments in the copper concentration showed strong HOMO delocalization near 2–3 adjacent copper cations with no further delocalization as the copper concentration increased. Based on the obtained data, PL mechanisms were described as the recombination of a photogenerated hole localized near a Cu atom with an electron in the CB, further supporting the idea of the recombination related to a copper defect.[74]

At the same time, van der Stam *et al.*[75] investigated the effects of electron injection and extraction on trap distribution in $CuInS_2$ through spectroelectrochemistry.[75] Their findings revealed that Cu^+ traps are solely responsible for radiative recombination processes, contrary to the notion that Cu^+ and Cu^{2+} traps contribute to the emission. It was mentioned that Cu^{2+} traps require hole trapping to enable radiative recombination. van der Stam's experiments showed that electron injection into the material increased the PL of $CuInS_2$. This behavior was attributed to the reduction of Cu^{2+}, which acts as non-emissive "dark centers", to Cu^+; the latter functions as emissive "bright centers". Conversely, oxidizing the sample caused a decrease in PL intensity.[75] The schematic of the proposed mechanism of dark and bright centers is shown in Fig. 3c. The reduction of Cu^+ not only enhanced PL intensity but also altered its bandwidth and peak position due to the elevation of the Fermi level. This process can be better understood by considering that the activated Cu^+ can participate in radiative recombination by trapping photogenerated holes, whereas Cu^{2+} promotes non-radiative Auger-assisted trapping, rendering those traps non-emissive.[75] The authors aimed to quantify the concentration of Cu^{2+} atoms in the material, but they concluded that the concentration was too low to be detected using *in situ* XANES techniques. As noted, the precise localization of these traps remains an open question.[75]

Fuhr *et al.*[33] discussed that both oxidation states are responsible for PL, in contrast to van der Stam *et al.*,[75] who indicated that Cu^{2+} states are non-emissive, as electrochemical oxidation of $CuInS_2$ leads to a decrease in the material's emissivity.[75] Fuhr *et al.*[76] gave further insight into these matters in their subsequent work, published in 2020, where, despite copper being present in two different oxidation states, both can participate in the emission processes through various mechanisms. Cu^+ with a filled 3d^{10} shell only requires trapping a photoexcited VB hole before recombination. On the other hand, Cu^{2+} with a 3d^9 shell can directly participate in emission by trapping a CB electron, as it already has a hole. However, the photoexcited hole must leave the valence band (VB) state for the Cu^{2+} cations to trap the conduction band (CB) electron radiatively. Their study further illustrated the presence of both oxidation states through magnetic dichroism, where samples with filled 3d^{10} shells are nonmagnetic, while those with 3d^9 configurations, which possess unpaired spins, showed magnetic behaviour. As stated in their work, both mechanisms can coexist, and the dominance of one over the other depends on the sample's stoichiometry. Furthermore, it was suggested that the location of the defect where Cu^+ states are antisite Cu_{In}–In_{Cu}, while Cu^{2+} emerges as charge compensation for copper-deficient samples that are rich in copper vacancies.[76]

Over the last years, single-nanocrystal analysis has been essential to understand that the properties like the broad PL emission correspond to an average emission arising from a population of QDs with distinct emissive properties. As shown in the work of Hinterding *et al.*,[77] the difference in the excitation spectra of individual $CuInS_2$ QDs compared to their ensemble is supported by: the variation among QDs, which can arise due to differences in composition, size, and shape, as well as spectral diffusion analysis of the QDs, which indicates a recombination of a delocalized electron with a localized hole. The authors proposed that the hole can be localized on the Cu^+ belonging to the crystal lattice, or on one specific Cu site near a defect, or surface charge. The latter mechanism was preferred as the PL peak position and lifetime measurements supported the idea of the hole localization in a preferential Cu site based on QDs properties like composition, surface ligands, and shape,[77] The optical properties of individual nanocrystals analyzed can be observed in Fig. 3d, along with a schematic of hole localization.

Later in 2021, Xia *et al.*,[78] through single low temperature QD spectroscopy, analyzed the differences in the spectral features of individual ZnS/$CuInS_2$ QDs, where two types of emission features were observed. Firstly, a classic broad emission (FWHM ~210 meV) again attributed to recombination of a delocalized CB electron with a localized copper-related hole, as well as a sharp, narrow (emission FWHM ~1 meV), which was attributed to a band edge exciton recombination. Both types of emission were not observed in the same QD, theorizing that the position of the Cu traps defines the PL mechanism. When the Cu traps are located near the QD surface band edge, recombination dominates due to better passivation. On the other hand, when Cu traps are located at the core, a free-to-bound recombination dominates due to incomplete passivation.[78]

Cu^{2+} action in the PL mechanism was reinvestigated by Harchol *et al.*,[79] where spin Hamiltonian simulations in $CuInS_2$/CdS indicated a strong coupling of the photogenerated hole

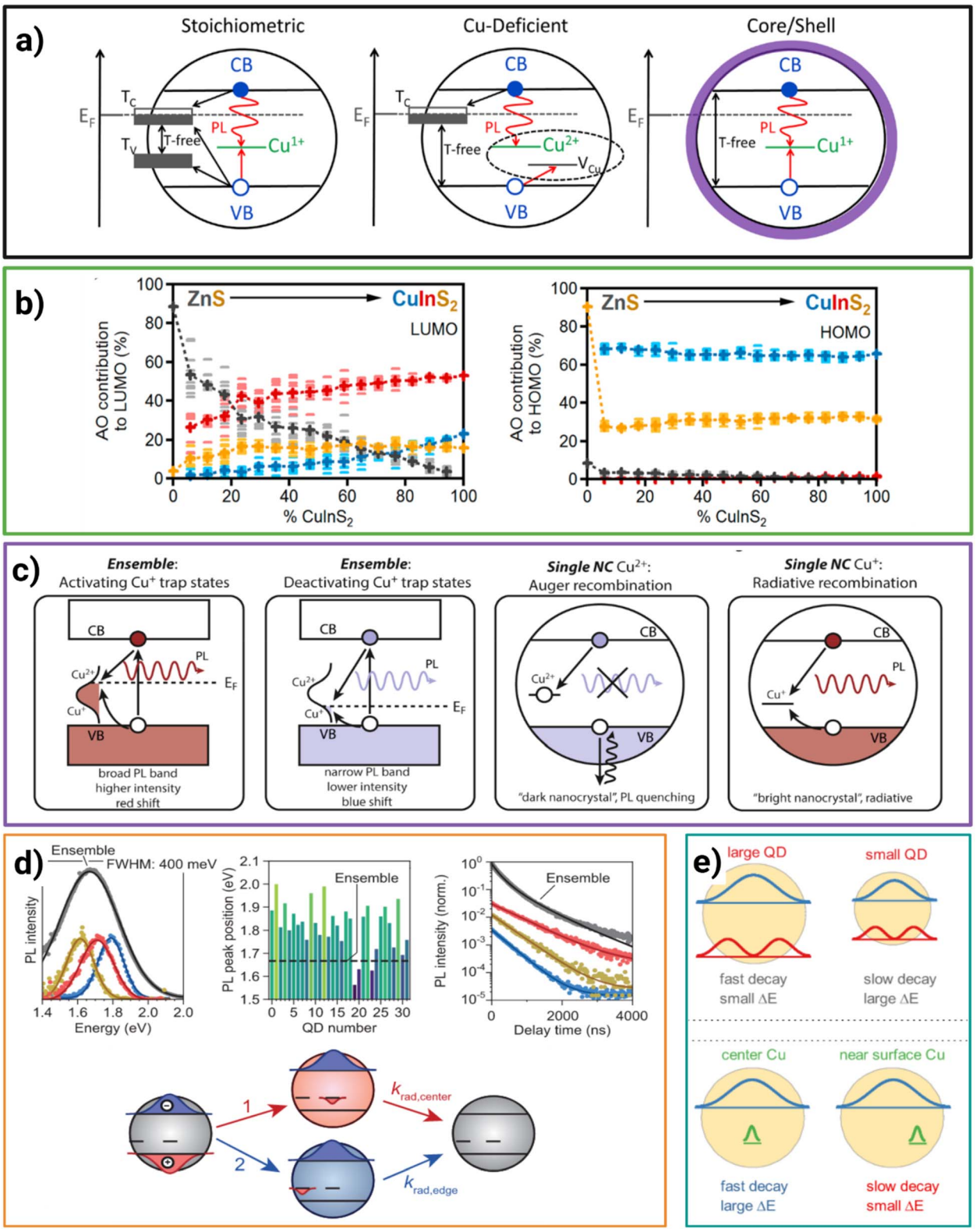

Fig. 3 (a) Proposed emission pathways for stochiometric, copper-deficient, and core–shell $CuInS_2$, adapted with permission from ref. 34. Copyright 2017 American Chemical Society. (b) LUMO and HOMO percentage of contribution of Cu and Zn for ZnS cluster with increased content of Cu and In, adapted with permission from ref. 73. Copyright 2018 American Chemical Society. (c) Proposed mechanisms for Cu^+ and Cu^{2+} trap states in ensemble and single $CuInS_2$ crystals, adapted with permission from ref. 74. Copyright 2018 American Chemical Society. (d) Optical properties of individual $CuInS_2$/CdS and schematic description of hole localization on the individual crystal. Adapted with permission from ref. 76. Copyright 2021 American Chemical Society. (e) Schematic of differences between PL decay rates based on QD size and trap localization, adapted with permission from ref. 79. Copyright 2023 American Chemical Society.

with a Cu^{2+} trap, suggesting that the recombination involves a self-trapped exciton at a photogenerated Cu^{2+}.[79] Further confirmation of a free-to-bound type of PL mechanisms was provided by Szymura *et al.*[80] At low temperatures, the PL decay rate decreased, which, as described by the authors, wouldn't be compatible with an excitonic recombination. Additionally, the application of a magnetic field did not affect PL lifetimes as compared to binary chalcogenides, which suffer from PL lifetime reduction. The authors also showed that size and copper trap localization are essential components in defining PL dynamics, where large QDs suffer from fast decay compared to smaller counterparts. Moreover, when Cu traps are positioned near the surface, the PL decay is slower, while traps in the core lead to faster decay. In contrast, core-located traps show fast decay[80] (Fig. 3e).

In summary, while the consensus points towards a free-to-bound mechanism involving Cu-based trap states, the exact role of Cu^{2+} *versus* Cu^{+} and the location of these traps (core *vs.* surface) remain as open questions.

4. Core shelling

As mentioned in the introduction, a limiting aspect of these materials in applications such as light-emitting devices is their low PLQY, which is typically ≤15%.[36,38,57,58,69,71,81] The low PLQY results from significant non-radiative recombination, driven by the high abundance of defects within the crystalline lattice.[81] To address this limitation, passivation strategies involving alloying, or shelling the QDs are common approaches employed to significantly increase the PLQY values.[26,58,68,82–86] These strategies not only mitigate material defects, thereby enhancing PLQY, but also provide a protective layer against environmental degradation caused by oxidation, prolonging the stability of the optical properties.[36] Among the materials frequently used for forming core–shell structures, ZnS stands out as one of the most used compositions, thanks to a zinc blende structure possessing a lattice mismatch of 2–3%, making it well-suited for epitaxial growth over a $CuInS_2$ core.[36,81,87] In core–shell processes, several mechanisms can occur based on the reactivity of Zn and S precursors and the synthetic conditions used. This is illustrated in Fig. 4a, where processes such as etching, epitaxial growth, cation exchange, and nucleation of ZnS can be involved.[81]

While ZnS is also often used for shelling $CuInSe_2$, studies have proven a better effect of passivation on $CuInSe_2$ due to a minor lattice mismatch of approximately 2% compared to ZnS (4–6%),[58] offering better optical properties as seen in Fig. 4b. However, the use of ZnSe has been less extensively reported, primarily due to the greater complexity associated with selenium precursors. This is in contrast to sulfur precursors like DDT that are commonly employed in shelling processes[71] alongside various zinc-based precursors (*e.g.*, ZnAc,[36,51,68,88,89] $ZnCl_2$,[71] ZnI_2,[81] $Zn(St)_2$,[32,81,82,90,91] and $ZnEt_2$ (ref. 58)).

ZnS has been demonstrated to improve PL on multiple occasions, increasing the PLQY value up to ~92.1%, as achieved by Liu *et al.*,[36] producing optical films with strong emission in the infrared region of the spectrum as seen in Fig. 4c; other examples are shown in Fig. 4d–f, where PL properties are enhanced as a function of shell time, or the amount of ZnS layers applied, achieving materials with emission in a broad range of colours. The introduction of a shell layer has brought significant improvements to shelf life, with reports of up to 6 months at 4 °C, accompanied by negligible loss of PL.[92] Additionally, optical films prepared with $CuInS_2$/ZnS have demonstrated good stability over a period of 1 month under ambient conditions. Another LED was reported to maintain 90% brightness over 30 days if stored in a glove box.[71] In Lian *et al.*'s.[93] work, the core–shell could maintain 84.2% PL after 2 months, while the core $CuInSe_2$ samples' PL only lasted 6 days.[93]

ZnS possesses a bandgap of 3.68 eV, which is wider than that of $CuInS_2$ or $CuInSe_2$, making it a suitable material for the growth of a type-1 core–shell. As such, it is ideal for applications like light-emitting devices[36] and solar concentrators, which require a high PLQY while maintaining the advantages of $CuIn(S, Se)_2$, namely, a large Stokes shift. However, it is commonly reported that either alloying or the shelling process results in a blue shift of the PL spectra, making it possible to produce different structures emitting from the red to green regions of the spectrum,[26,58,68,82–86] although it is still possible to maintain a low degree of blueshift.[36]

The PL of $CuIn(S, Se)_2$ QDs significantly improves *via* the epitaxial growth of a ZnS shell, as evidenced by temperature-dependent PL studies and transient absorption (TA) measurements, where the ZnS shell inhibits electron–phonon interactions and Auger recombination processes by effectively passivating particle surface defects.[36] Reduction in nonradiative recombination is also mentioned in the works of Yamashita *et al.*[88] and Xia *et al.*,[94] where the growth of a ZnS shell protects the surface of the core, suppressing surface trap-mediated recombination.[88,94] More recently, Xia *et al.*,[78] used low-temperature single QDs spectroscopy in a sample of $CuInS_2$/ZnS, where two subpopulations of QDs with different PL behaviour were found in their study. One subpopulation exhibited sharp, resolution-limited emission lines attributed to the zero-phonon recombination of a long-lived band-edge exciton, resulting from the ZnS shell's perfect passivation. In contrast, the other population possessed broad spectra attributed to the self-trapping of holes by defects arising from non-well-passivated QDs.[78]

Identifying a core–shell structure formation in multiple studies is often associated with increased size distribution of QDs.[36,58,84,92,93,95,96] This size increase can be attributed to the deposition of layers of ZnS or ZnSe, whose monolayer thicknesses are approximately 0.31 and 0.33 nm, respectively.[82] Elemental analysis, such as EDS coupled with HRTEM, can serve to identify the elemental distribution, which can be associated with shell formation, as reported by Liu *et al.*[36] PL and absorption spectra can also provide insights: an increase in PLQY with minimal PL blueshift indicates successful core–shell formation rather than an alloying process.[58] However, as Darren Neo *et al.*[82] noted, PL and absorption spectra alone cannot fully distinguish between passivation *via* alloying and core–shell formation.[82]

Core–shell formation with ternary chalcogenides like $CuInS_2$ has also been explored, as demonstrated in the work by Ning *et al.*[38,69] However, the PLQY achieved in these studies was not as

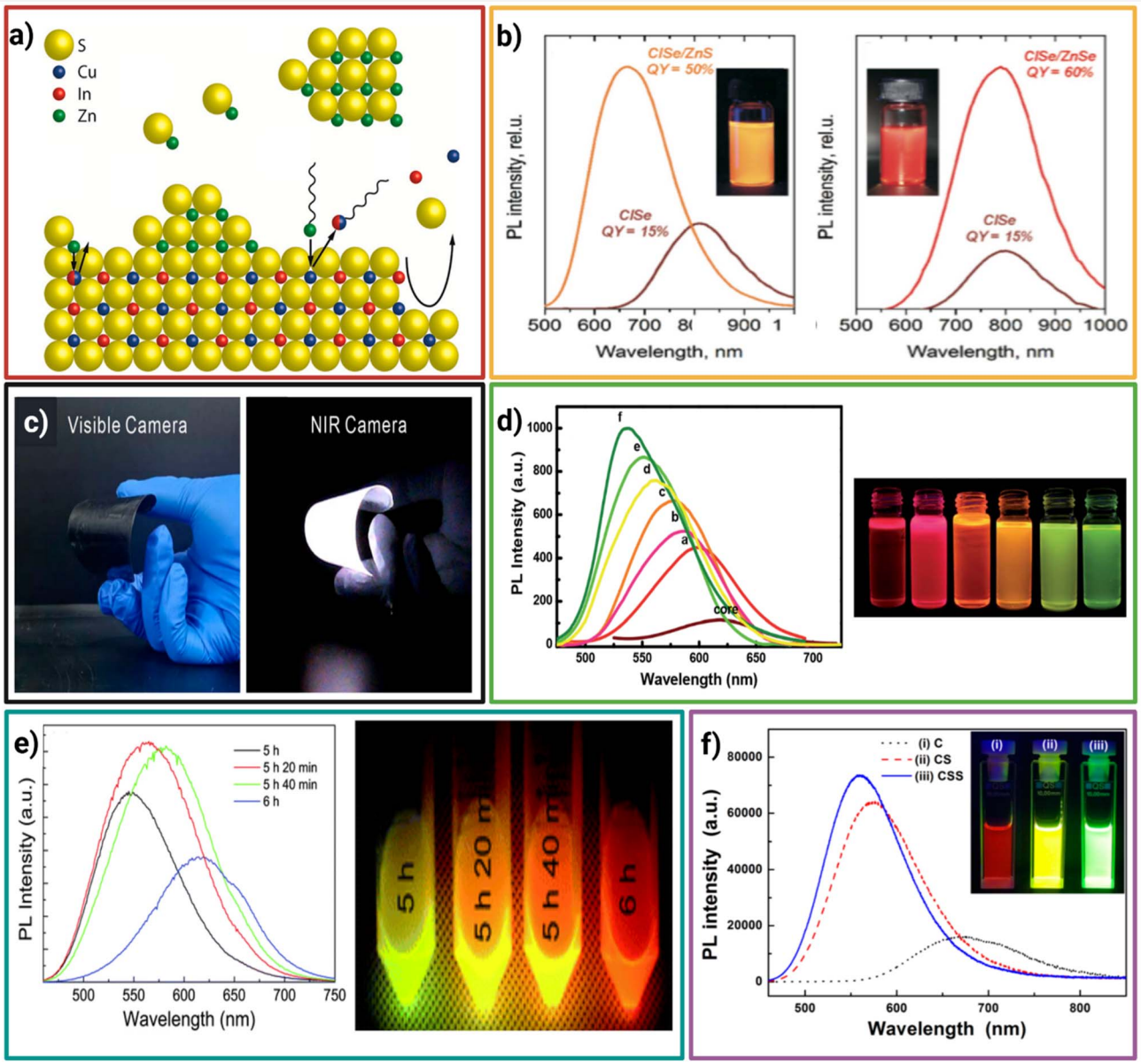

Fig. 4 (a) Chemical processes that can occur during the passivation of $CuInS_2$ with ZnS, where mechanisms like etching, epitaxial growth, alloying, cation exchange, and ZnS nucleation can occur, adapted with permission from ref. 80. Copyright 2018 American Chemical Society. (b) Differences in PL emission from $CuInSe_2$ samples core–shelled with ZnS and ZnSe, adapted with permission from ref. 56. Copyright 2013 American Chemical Society. (c) Infrared photographs of polymer films coated with ZnS/$CuInS_2$ quantum dots, adapted with permission from ref. 49. Copyright 2024 American Chemical Society. (d) Effect on PL emission of the amount of ZnS layers on $CuInS_2$ quantum dots alloyed with Zn, adapted with permission from ref. 67. Copyright 2019 The Royal Society of Chemistry. (e) Emission properties of ZnS/$CuInS_2$ under different reaction times, adapted with permission from ref. 85. Copyright 2011 The Royal Society of Chemistry. (f) Emission properties of $CuInS_2$ quantum dots with different increasing amounts of ZnS layers, adapted with permission from ref. 83. Copyright 2015 American Chemical Society.

high as in other works using ZnS shells, with a maximum PLQY of 20% reported for $CuInSe_2/CuInZnS_{2-x}Se_x$.[38] These findings suggest that further refinement of growth conditions and shell engineering could enhance the PLQY. Notably, their study demonstrated the successful generation of core–shell structures exhibiting quasi-type I ($CuInSe_2/CuInZnS_{2-x}Se_x$), type II ($CuInSe_2/CuInS_2$), and quasi-type II or type II ($CuInSe_2/CuInS_{2-x}Se_x$).[38] Additionally, a more focused investigation on the shell growth of $CuInSe_2$ revealed that the choice between chalcopyrite and wurtzite shell structures depends on the number of precursors supplied during the shell formation process.[69]

5. Advances in the synthesis of $CuInX_2$

5.1. Synthesis

Currently, there are several methods for synthesizing $CuInX_2$-based nanomaterials, and colloidal synthesis has gained

considerable popularity. A solution-based colloidal synthesis refers to a synthesis that results in nanoparticles or nanomaterials existing in colloid form. A colloid is best defined as a homogeneous amorphous substance in which insoluble larger molecules are dispersed. Therefore, the particles do not agglomerate and settle.[97] Colloidal synthesis is thus a versatile tool that eliminates the use of expensive equipment for the synthesis of nanostructures; this has allowed interesting and unique pathways of synthesis, like the use of bubble wrap (Fig. 5a) as a media container.[98] It has been shown that colloidal $CuInS_2$ nanocrystals embedded within ZnS rods can be produced *via* a multistep, seeded growth process. Xia *et al.*[94] have demonstrated that an original template consisting of $Cu_{2-x}S$ can be used to obtain $CuInS_2$ nanocrystal seeds. This is achieved through a cation exchange procedure involving topotactic partial exchange of Cu^+ for In^{3+} in the $Cu_{2-x}S$ template. A ZnS rod shell is formed around the $CuInS_2$ seeds, resulting in colloidal $CuInS_2$/ZnS heteronanorods.[94] In binary

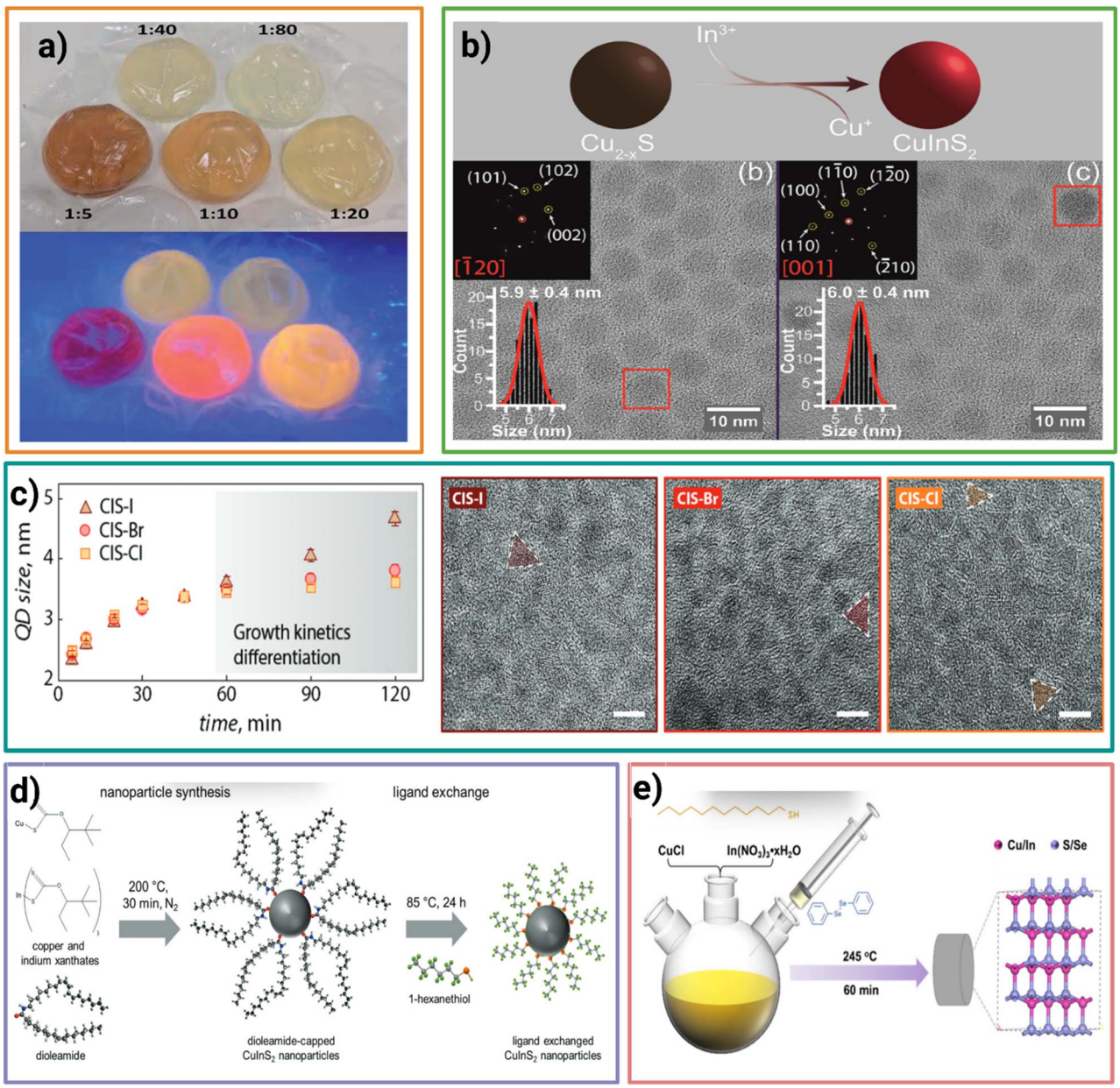

Fig. 5 (a) Synthesis of $CuInS_2$ QDs in bubble wrap, adapted with permission from ref. 96. Copyright the Royal Society of Chemistry 2019. (b) Production of $CuInS_2$ nanocrystals through cation exchange, starting from $Cu_{2-x}S$, adapted with permission from ref. 54. Copyright American Chemical Society 2018. (c) Effect of halide ions (I, Cl, and Br) in the growth dynamics of $CuInS_2$ and their respective TEMs, adapted with permission from ref. 100. Copyright The Royal Society of Chemistry 2020. (d) Use of metal xanthanates for the synthesis of $CuInS_2$ nanoparticles and the ligand exchange to hexanethiol, adapted with permission from ref. 101. Copyright The Royal Society of Chemistry and the Centre National De La Recherche Scientifique 2019 (e) use of diaryldiselenides as Se source for the synthesis of $CuIn(S_xSe_{1-x})_2$, adapted with permission from ref. 37. Copyright American Chemical Society 2024.

chalcogenides, cation exchange has proven to be a reliable method to produce ternary compositions with little-to-no change in size or morphology[56] as seen in Fig. 5b. In another study, Pang *et al.*[99] demonstrated a simple solution-based synthesis method for producing $CuInSe_2$ nanocrystals. This was done using CuCl, $InCl_3$, and Se powder. The precursors are mixed in a three-neck round-bottom flask and heated under vacuum, followed by the addition of a stabilizing ligand to form colloidal $CuInSe_2$ nanocrystals.[99] In a solution-based synthesis, one precursor may be heated to high temperatures (>100 °C) in a given solvent to ensure complete dissolution. Then, a second precursor, in a process known as the hot injection synthesis, is added to the solution to initiate the reaction.[100] In the general solution-based synthesis of $CuIn(Se, S)_2$ materials, octadecene is a very common solvent due to the reduction of elemental sulfur, or selenium for incorporation into the material. Still, it can also come with a significant disadvantage that should be recognized.[104] It has been found that octadecene spontaneously polymerizes under ordinary synthesis temperatures (120–320 °C), and typical purification procedures (precipitation/redispersion, size exclusion chromatography) fail to remove the impurity.[104] Dhaene *et al.*[104] have shown that saturated solvents can be used to replace octadecene when it does not participate in the reaction, or surface functionalization can be used to easily separate the materials from the polymerized impurity in cases where octadecene does indeed participate in the reaction.[104] Addition of halogens has also been utilized as a size modulator showing different results depending on the halogen used as seen in Fig. 5c. The addition of halides can be achieved through the use of metal precursors, such as CuCl, CuBr, and CuI, where the Br and Cl ions have been shown to reduce growth kinetics after 45 minutes compared to I.[105] Perner *et al.*[106] have utilized copper and indium xanthanates, which both contain their respective metals, including sulfur, as shown in Fig. 5d. Their reaction at higher temperatures, in combination with dioleamide, allowed the growth of $CuInS_2$ nanoparticles, which then underwent a ligand exchange with hexane thiol to improve charge transfer.[106]

5.2. Growth mechanisms

The growth mechanisms of $CuInS_2$ and $CuInSe_2$ depend on the type of metal and non-metal reagents used in the synthesis. For $CuInS_2$. As reported by Gromova *et al.*, a basic synthesis involving CuI, indium acetate, and DDT initially leads to the formation of lamellar structures composed of Cu, In, I, and thiolate species at 100 °C. Further heating destabilizes these 2D structures, triggering C–S bond cleavage, which initiates the nucleation of $CuInS_2$ in the chalcopyrite phase commonly observed in syntheses using DDT. Throughout the reaction, the In/Cu ratio remained close to 1 : 1. Surface analysis shows that colloidal stabilization of the nanoparticles arises from a double-layer structure composed of thiolates and didodecyl sulfide molecules.[70]

In syntheses involving elemental selenium, the mechanism of nanocrystal formation depends strongly on the ligands used, as they influence the availability and reactivity of the metal precursors. In a study by Kar *et al.*, the effects of coordinating *versus* non-coordinating solvents such as OLA and octadecene were compared. When OLA was used, MALDI analysis revealed multiple OLA derived species with varying carbon chain lengths (from C_{17} to C_9), as well as a chlorinated OLA derivative. FTIR analysis further confirmed the presence of an alkylamine hydrochloride, suggesting that the metal precursors (*e.g.*, CuCl and InCl3) generate HCl *in situ*, which reacts with OLA to form its corresponding ammonium salt. XRD analysis of the nanocrystal products showed that under these conditions and with elemental selenium, the formation of $CuInSe_2$ proceeds *via* intermediate binary phases of CuSe and InSe. In contrast, when non-coordinating solvents such as ODE or octadecane were used, chlorinated derivatives were also observed. However, the binary phases formed under these conditions were $Cu_{2-x}Se$ and In_2Se_3, rather than CuSe and InSe.[107]

A deeper look into the $CuInSe_2$ growth mechanism has not been developed as extensively as for $CuInS_2$, although it is theorized that the formation of lamellar structures with the metal components is also involved when ligands such as dodecaneselenol are used as the selenium source.[108] This was shown by Hernández-Pagán *et al.*, whose low-angle X-ray diffraction patterns revealed periodic peaks similar to those observed at initial stages in syntheses involving Cu precursors and thiolate ligands.[108]

For syntheses involving the combination of oleic acid and OLA, it has been found that both ligands react to form di-oleylamine, which further stabilizes the metal precursors.[106] However, no specific mechanism for the formation of either $CuInS_2$ or $CuInSe_2$ has been proposed. Although it has been mentioned that in reactions involving metal xanthates, the formation of the semiconductor proceeds through a Chugaev reaction, the presence of ligands can alter the formation mechanism, as stated by Perner *et al.*[106]

$CuInSe_2$ formation often requires the use of a colloidally compatible Se precursor. Some syntheses still involve the use of phosphine-related chemicals, although new strategies have been under development to facilitate the synthesis of pure-phase $CuInSe_2$. One of the first attempts to develop a colloidally suitable precursor was the dissolution of elemental selenium in a mixture of OLA with DDT, where the latter was able to reduce the Se and induce the formation of Se–OLA complexes and didodecyl disulfide.[109] No particular mechanism of formation has been proposed involving this kind of precursor, although the presence of disulfides in the reaction can still act as sulfur precursors by undergoing homolytic cleavage, as observed in syntheses involving dialkyl diselenides.[108]

In addition to other selenium precursors, dialkyl diselenides have also gained high interest because of their colloidal stability and their capability of unlocking crystalline phases such as wurtzite. However, this will depend on factors such as bond strength, since several diorganyl diselenides have been shown to produce either the chalcopyrite or the wurtzite phase.[110] For example, Tappan *et al.* tested the differences between three different diorganyl diselenides and their outcomes in crystal phase formation. Among them, dimethyl diselenide and dibenzyl diselenide yielded the formation of the chalcopyrite

phase, although its formation wasn't direct and involved first the formation of a $Cu_{2-x}Se$ phase, which then required the diffusion of In^{3+} ions and the out-diffusion of $_{(1-x)}Cu$ cations. In contrast, diphenyl diselenide yielded the formation of the wurtzite structure, which first involved the formation of umangite (Cu_3Se_2), followed by the diffusion of In^{3+} and the out-diffusion of Cu^+ and Cu^{2+} in order to stabilize the charge of the final $CuInSe_2$ wurtzite crystal.[110] Tappan *et al.*'s findings indicated that the bond strength of the C–Se bond had more impact on the reactivity compared to the Se–Se bond, which showed a difference of 11.21 kcal mol^{-1} between the strongest and weakest diselenide bonds, diphenyl diselenide and dibenzyl diselenide, respectively. On the other hand, the C–Se bond dissociation strength had the greatest variation, being the strongest in diphenyl diselenide (64.65 kcal mol^{-1}), followed by dimethyl diselenide (57.18 kcal mol^{-1}), and finally (43.09 kcal mol^{-1}). In conclusion, these findings suggest that the formation of a more thermodynamically stable phase, such as chalcopyrite, is associated with diorganyl precursors having weaker C–Se bonds.[110]

Hernández-Pagán *et al.* also tested the differences between didodecyl diselenide and dodecaneselenol in the formation of binary CuSe.[108] The estimated C–Se bond energy of dodecaneselenol (67.8 kcal mol^{-1}) and didodecyl diselenide (55.4 kcal mol^{-1}) would suggest that the selenol reagent should induce the formation of a less thermodynamically favourable structure, while the weaker diselenide bond would favor the formation of a more thermodynamically stable structure. However, the results were contradictory, dodecaneselenol led to the formation of the cubic $Cu_{2-x}Se$ phase, while didodecyl diselenide yielded $Cu_{2-x}Se$ in the wurtzite phase.[108] The proposed mechanism involving dodecaneselenol suggested the formation of lamellar structures with the copper reagent, as observed in other copper/DDT reactions.[108] The formation of these structures, as well as copper withdrawing electron density from the Se atom, would then weaken the C–Se bond, facilitating the formation of the cubic phase. In contrast, although didodecyl diselenide has a weaker C–Se bond, it would still require the appropriate energy to first undergo homolytic cleavage before participating in crystal nucleation.[108]

Berends *et al.* also tested the outcome of dodecaneselenol in the synthesis of CuSe nanocrystals, yielding umangite, which was then treated through cation exchange to form $CuInSe_2$.[111] The difference in crystal phase between the two previously discussed works using dodecaneselenol can be attributed to the differences in the selected precursors and ligands involved in the synthesis: Hernández-Pagán tested the precursor along with octadecene,[108] while Berends *et al.* included the presence of trioctylphosphine oxide,[111] indicating that the chosen ligand influences the reaction mechanisms and thus the resulting crystalline phase.

A deeper look into the reactivity of dodecaneselenol with other commonly used ligands was also tested by Ho *et al.*, where the reaction of dodecaneselenol with ligands such as octadecene, OLA, OA, stearylamine, stearic acid, and dioctyl ether yielded CuSe nanocrystals in different phases such as cubic for octadecene, OA, stearic acid, and dioctyl ether; hexagonal for

Table 1 Summary of synthesis conditions for $CuInS_2$ and $CuInSe_2$ nanocrystals, including precursor types, ligand systems, reaction parameters, and resulting crystal phase and size

Material	Synthesis method	Precursors	Ligand/solvent	Max temp	Time	Crystal phase	Size	Ref.
$CuInS_2$	Solution-based/cation exchange	$InCl_3$ Copper(I) acetate *Tert*-dodecanethiol	1-Octadecene Tri-*n*-octylphosphine	180 °C	15 min	Wurtzite	Rods, length: 55.3 ± 3.3 nm, width: 24.6 ± 1.4 nm	101
$CuInSe_2$	Solution-based/hot injection	$In(OAC)_3$ CuI Se powder	OLA 1-Octadecene	200 °C	15 min	Chalcopyrite	15 nm	100
$CuInSe_2$	Solution-based/hot injection	$InCl_3$ CuCl Se powder	OLA Diphenylphosphine	240 °C	1 hour	Chalcopyrite	9.6 ± 1.1 nm	99
$CuInSe_2$	Solution based	$InCl_3$ CuCl Se powder	OLA	240 °C	10 min	Chalcopyrite	6.3 ± 1.5 nm	44
$CuInS_2$	Solution-based/hot injection	$In(acac)_3$ $Cu(acac)_2$ Trioctylphosphine oxide	OLA DDT *Tert*-dodecanethiol	310 °C	1 hour	Wurtzite	Oval nanoparticles, length: 42.78 ± 5.55 nm, width: 27.52 ± 3.06 nm	102
$CuInS_2$	Solution based	$In(NO_3)_3 \cdot 3H_2O$ $Cu(NO_3)_2$ Na_2S	Iminodiacetic acid Glycine	30 °C	1 hour	Chalcopyrite	20–100 nm	103

Table 2 Summary of ligand exchange strategies for $CuInS_2$ and $CuInSe_2$ nanocrystals, highlighting original and new ligands

Material	Original ligand	New ligand	Hydrophilic/hydrophobic phase	Temperature (°C)	Time	Ref.
$CuInS_2$ $CuInSe_2$	OLA	Mercaptopropionic acid	30% NaOH solution	Room temperature	2 h	52
$CuInS_2$	DDT	Mercaptopropionic acid	Diethylene glycol/tetradecane	160–220 °C	1 h	113
$CuInS_2$/ZnS	DDT/OA	Mercaptopropionic acid Cyclohexyl 3-mercaptopropionate	Ligand exchange is done directly after ZnS shell formation	250 °C	15 min	89
$CuInSe_2$	OLA/dyphenilphosphine	S^{2-}	Formamide/hexane	Room temperature	1 h	99
$CuInSe_2$	OLA	2,5-Dimercapto-1,3,4-thiadiazole 2-Amino-5-mercapto-1,3,4-thiadiazole	Ligand exchange is done after CuInSe film formation on the substrates	Room temperature	20 min	114
$CuInS_2$/ZnS	DDT	γ-(mercaptopropyl)trimethoxysilane	1-Hexyl-3-methylimidazolium chloride/ toluene	Room temperature	30 min	68
$CuInS_2$/ZnS	DDT	Dodecylamine, OLA	Ligand exchange was done after ZnS formation, 11-mercapto-1-undecano was used in the ligand exchange procedure	180 °C	30 min	115
$CuInSe_2$	OLA, diphenylphosphine	Trioctylphosphine, octanethiol	Ligands were exchanged with hydrophobic ligands, so the primary solvent was toluene in combination with the new ligands and iodine as an aiding agent for the exchange	Room temperature	Multiple times tested	116
$CuInS_2$	OLA, trioctylphosphine oxide, DDT	Methylbenzenethiol (4-MBT)	Dried $CuInS_2$ was mixed with 20 times the amount of 4-MBT	180 °C	72 h	66
$CuInS_2$/ZnS	DDT, OLA, OA	6-Mercaptohexanol	Ligand exchange is done after ZnS formation	180 °C	15 min	117
$CuInSe_2$	OLA	3-Mercaptopropionic acid	Chloroform/deionized water, pH adjusted to 8–9	Room temperature	2 h	25

stearylamine; and a mixture of hexagonal and umangite for OLA. Reaction products were also identified among the different combinations of ligands and dodecaneselenol, including the formation of species such as dialkyl selenides, dialkyl diselenides, hydrogen selenide, and selenoethers, depending on the type of ligand used.[112]

Although the previously reported articles focus on the formation of copper selenide binary structures, their findings can help guide the direct synthesis of ternary chalcogenides such as $CuInSe_2$ without requiring cation exchange, when using less common selenide precursors such as selenols and diorganyl diselenides. A comprehensive list of recently reported syntheses for $CuInX_2$ materials is presented in Table 1, specifying the type of reaction used for their synthesis, along with the reported size and crystal phase.

5.3. Strategies for defect control

Defects are described as changes to the arrangement of atoms from their ideal sites in the crystal structure of their bulk solids.

The existence of defects allows solids to have different properties. Defect chemistry enables various electronic, thermal, optical, magnetic, catalytic, and mechanical properties in materials; therefore, it is essential to understand how to control such defects.[118] Li *et al.*[119] have shown that shallow defects in $CuInS_2$ QDs help capture charge carriers without affecting their transport, while deep defects capture charge carriers and entirely confine them, which can be consequential for chemistry related to photocatalytic hydrogen production. By growing ZnS on the surfaces of the QDs, the authors showed that the deep defects become passivated. When choosing the chemical source of a metal used in synthesizing these materials, it is essential to be meticulous. Enkhbat *et al.*[120] have found that acetate sources resulted in high defect densities and many Cu_{Zn} antisites. In contrast, using nitrate and chloride sources improved solution stability and speaks to the importance of source selection in dictating defect control.

5.4. Role of ligands and surface engineering

Just as defects are essential for dictating the properties of a material, so are the ligands attached to their surfaces. It has been previously demonstrated that surface ligands can significantly influence surface morphologies, particle sizes, solubilities, optical properties, and band structures.[121–125] Ligands can enable the colloidal stability of nanomaterials through electrostatic and/or steric interactions. Nanomaterials are often said to be stabilized by such ligands and repeatedly remain a colloid due to the electronic repulsive forces applied between the charged ligands and the repulsive physical steric interactions between non-charged ligands.[126] An organic ligand is generally introduced as an organic solvent throughout the reaction progression. The solvent begins to envelop the surface of the crystal seeds, forming organic ligands that regulate the material's size and morphology by controlling the growth of the seeds.[127] The length of the ligands also controls the insulating properties, directly affecting the charge transfer between the QDs. Liu *et al.*[59] have shown that a long-chain OLA ligand can be incorporated on $CuInSe_2$ QDs surfaces by mixing all precursors with OLA in a heated flask under an inert atmosphere.[59] Zhang *et al.*[25] have shown that the OLA ligand can be exchanged with 3-mercaptopropionic acid (MPA) *via* a ligand exchange procedure. The materials were used as hole transport materials in perovskite solar cells, and it was found that the PCE increased from 7.19% to 8.59% when the OLA capping ligand was replaced with the short MPA ligand owing to its weaker insulating properties.[25] It's also been found that commercial-grade OLA contains impurities. Thus, depending on the desired purity of the formed ternary material, it is essential to either purchase high-purity OLA, or simply carry out in-house purification to ensure that the ligand solution is as pure as possible.

Long-chain ligands, such as OLA, have also been found to be a source of carbonaceous impurities, which can leave a discrete residue between the absorber layer and the back contact in photovoltaic devices, thereby affecting grain growth. Ellis *et al.*[128] have developed an exhaustive hybrid organic/inorganic ligand exchange procedure to completely strip the OLA ligand and replace it with the inorganic capping agent diammonium sulfide ($(NH_4)_2S$), improving grain growth.[128] Alternatively, Hayes *et al.*[129] have found that using *N*-methyl-2-pyrrolidone as an alternative to long-chain ligands such as OLA improves grain size and reduces carbonaceous residues, presumably due to the reduced carbon content.[129] Table 2 presents recent works.

6. Integration of $CuInX_2$ in solar energy conversion devices

6.1. Solar cell devices

As discussed in the previous section, ternary chalcogenides like $CuIn(S, Se)_2$ have garnered attention in the solar energy conversion field due to their high absorption coefficients, tunable band gaps, high defect tolerance, and low toxicity compared to lead halide perovskites.[29,130,131] However, ternary chalcogenides have also been applied in conjunction with perovskite-based solar cells, thereby increasing energy conversion.[25,130,132–138] Although ternary chalcogenides offer advantages in terms of sustainability and device performance by extending the absorption spectrum, several key challenges still limit their broad application in solar energy conversion devices. First, their high defect density facilitates nonradiative recombination, which reduces charge separation efficiency.[133,139] Second, controlling size and stoichiometry remains difficult; most reported syntheses yield broad size distributions, which can lead to underperformance, particularly because smaller quantum dots may limit the open-circuit voltage V_{oc} during charge transfer.[140] Third, common colloidal syntheses rely on bulky surface ligands to maintain colloidal stability. These ligands can hinder charge transfer and often require a ligand-exchange step.[25,129] However, the success of this exchange strongly depends on the type of ligand used; for example, thiolated ligands like DDT bind tightly to the nanocrystal surface and are difficult to replace.[113] In addition, these materials can undergo environmentally driven degradation, especially at their interfaces with other device components,

further impacting device stability and performance.[141] Despite these limitations, ternary chalcogenides remain attractive for use in solar cells as either light-absorbing layers or hole transport materials due to their tunable optoelectronic properties. Today, the PCE of solar cell devices using $CuInS_2$ or $CuInSe_2$ varies significantly depending on the device architecture. Quantum dot-sensitized solar cells, integrating $CuInS_2$, have achieved PCE values of 12.21% (ref. 142) and 15.52%.[143] While tandem configurations with perovskites have achieved efficiencies of up to 29.9%.[138] Other examples of reported devices and their performance metrics are presented in Table 4.

Notably, some of the highest PCEs for copper chalcogenides have been achieved through costly processes like co-evaporation,[144] or vapor deposition.[129] Nowadays, colloidal synthesis of nanomaterials has become a popular method for fabricating $CuInX_2$ nanomaterials, offering the versatility of incorporating these materials through various methods, such as spin coating or dip coating, which are preferred in lab-scale applications as they don't require costly equipment. However, the main drawback regarding these methods is the amount of waste material generated in producing thin films. In spin coating, part of the solution is expelled from the substrate due to the centripetal/centrifugal forces, and dip coating techniques involve preparing enough ink to fully cover the substrate.[145] Although adequate, the actual spin velocity provides versatility in optimizing device performance based on layer thickness.[146]

In addition to deposition variables, the performance of copper chalcogenides is influenced by the synthesis process, where variables such as reagents and ligands can either enhance or limit their performance. For instance, in the colloidal synthesis of nanoparticles, ligand selection for solar energy conversion devices should be considered in the design process, as it can dramatically impact the device's performance. Particularly for solar cells, performance metrics vary depending on the functional groups and the length of the ligand.[72] In QD-sensitized solar cells, it is essential to achieve full coverage of the metal oxide electrode to avoid charge recombination with the electrolyte.[147] However, common synthetic routes use ligands like OAm, OA, and DDT, which are about 2.2 nm long. These ligands limit the packing density of the QDs. This makes further ligand exchange necessary to replace them with smaller ligands, which increases charge mobility,[25] improves packing density and enhances the light absorption capacity of the film[72] Shorter ligands like hexanethiol (HT)[106] or MPA whose length is around 0.7 nm are preferred to secure a higher QDs density on the surface of selected electrodes and higher coupling to the surface.[72] Inorganic ligands such as SCN^{-1} whose length is ~0.22 nm are also common to further increase the packing density of QDs.[147] The change in surface ligand has been shown to increase PCE from 6.2% (OAm) to 9.0% and 9.4% for MPA and HT, respectively. This is associated with higher packing and thus higher absorption capacity, elevating the J_{sc} to values of >26 mA cm^{-2}.[72] Dual ligand coverage has also been explored using MPA and inorganic ligands such as SCN^-, Cl^-, B^-, I^-, S^{2-}, and $S_2O_3^{2-}$. Among these, pairing MPA with SCN^- resulted in higher QD deposition on TiO_2. This improved film absorption and increased the PL decay lifetime from 17.10 ns (MPA-capped) to 44.94 ns (MPA, SCN^- capped). This led to the highest tested cell performance, with a certified PCE of 16.10% in a liquid-junction QD solar cell (Fig. 6a).[147] Other studies have substituted OAm with shorter ligands, such as *N*-methyl-2-pyrrolidone, in an effort to minimize the carbon residue left after the selenization of $CuInGaS_2$ films. This resulted in better grain formation (Fig. 6b) in conjunction with Na, as compared to OAm-capped nanoparticles, thereby increasing device performance metrics.[129] Other strategies to improve packing density involve secondary depositions of the QDs, as demonstrated by Song *et al.*[143] A pretreatment of the QDs-sensitized TiO_2 with metal oxyhydroxides allows better incorporation of the second layer of QDs with no interference of the light absorption[143] (Fig. 6c). Polymer heterojunctions using PCDTBT (poly[[9-(1-octylnonyl)-9*H*-carbazole-2,7-diyl]-2,5-thiophenediyl-2,1,3-benzothiadiazole-4,7-diyl-2,5 thiophenediyl]) in devices where the active layer is composed solely of a mixture of $CuInS_2$ nanocrystals and the polymer, with varying ratios of polymer and $CuInS_2$, have been demonstrated to affect the PL properties of the material. However, its PCE was relatively low, 0.23% (ref. 106) (Fig. 6d).

In other studies, increasing the amount of OAm in the synthetic procedure has also increased the PCE of perovskite PV prepared with $CuInS_2$ as the hole transport layer. Higher concentrations of OAm led to bigger and less covered QDs, which are believed to have fewer defects, thus avoiding non-radiative recombination pathways.[135] Although ligands like OAm and HT have shown longer electron transfer times in Zn:$CuInSe_2$ (20 ns), care must be taken to assume both ligands would perform inferior to MPA with faster electron transfer times of 0.35–3.5 ns, as demonstrated by HT, which achieves similar internal quantum efficiency values compared to MPA-capped QDs.[72]

As previously mentioned, compositional variations of either Cu/In or S/Se in mixed systems significantly influence the optoelectronic properties, making the study of such variations particularly interesting for improving solar cell efficiency and understanding charge dynamics.[52,153,154] Although several references suggest that copper-deficient materials achieve better PCE values, stoichiometric materials should outperform them due to their lower defect density and higher mobility.[27] Furthermore, PL has recently been described as a mechanism involving Cu^{2+} and Cu^{1+}, whose density depends on sample stoichiometry. Samples rich in Cu^+ traps (stochiometric) benefit solar conversion devices like solar cells by extending absorption in the intragap region, improving J_{sc} with little effect on V_{oc} because of fast trapping of the valence hole. On the other hand, samples rich in Cu^{2+} traps should outperform their counterparts in luminescent solar concentrators as the intragap absorption of Cu^+ is less, thus preventing self-absorption as described by the findings of Fuhr *et al.*[76] Suresh *et al.*[153] accomplished this as the stoichiometric samples of $CuInS_2$ surpassed the performance metrics of copper-deficient devices.[153]

Wang *et al.*[52] investigated the impact of varying the Cu/In ratio on the formation of $CuInS_2$ QDs passivated with ZnS. This was achieved by soaking the generated films in a $Zn(Ac)_2$

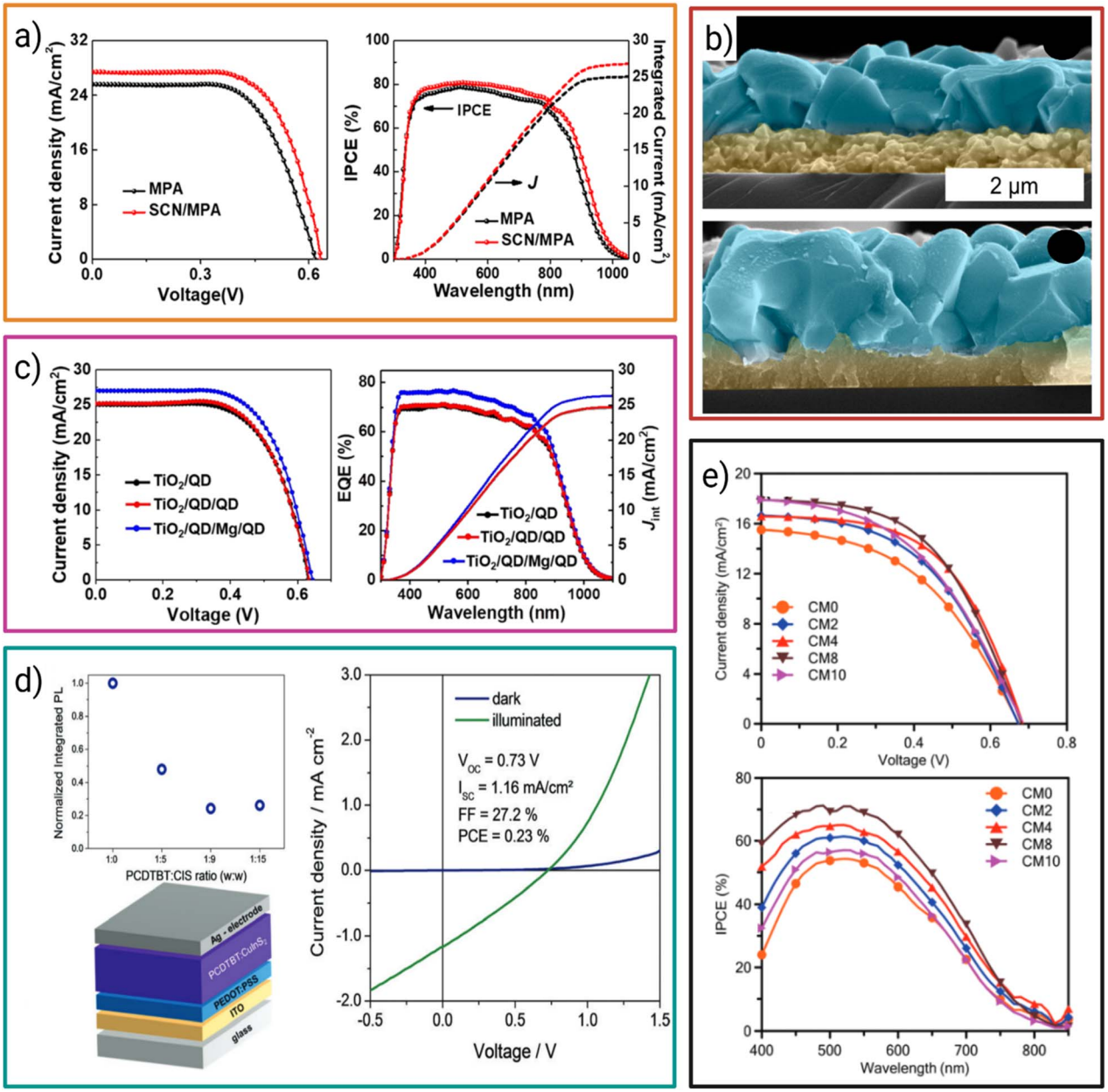

Fig. 6 (a) J–V curves and IPCE curves of QDSCs with single (MPA) and dual (MPA/SCN) ligands, adapted with permission from ref. 152. Copyright 2022 American Chemical Society. (b) Side view SEM images of $CuInS_2$ capped with N-methyl-2-pyrrolidone (top) and oleylamine capped (bottom), adapted from ref. 116. Copyright 2024 American Chemical Society. (c) J–V and IPCE curves of devices with single, double deposition of QDs and magnesium oxyhydroxide layer (Mg), adapted from ref. 143. Copyright 2021 American Chemical Society. (d) Effect of PCDTBT/$CuInS_2$ ratio on PL properties, device architecture, and corresponding J–V curves, adapted from ref. 101 with permission from the Centre National de la Recherche Scientifique (CNRS) and the Royal Society of Chemistry. (e) Effect of magnesium doping concentration on the I–V curves and IPCE curves of $CuInSe_2$ sensitized-TiO_2 solar cell, adapted from ref. 144 with permission from the Royal Society of Chemistry.

and Na_2S solution. Key performance factors, such as the open-circuit voltage (V_{oc}), were found to be influenced by the Cu/In ratio. Copper-deficient samples exhibited higher V_{oc}, contributing to an increased fill factor (FF) and PCE.[52] Interestingly, the short-circuit current density (J_{sc}) did not follow a clear trend with decreasing copper content. For example, a Cu/In ratio of 1 : 4 delivered a PCE of 8.54%, whereas a ratio of 1 : 5 resulted in a lower PCE of 6.95%. Further analysis, including time-resolved PL and electrochemical impedance spectroscopy, suggested that the improved performance in copper-deficient samples was due to the inhibition of charge recombination at the solar cell interface. This effect was attributed to a reduction in defect states, highlighting the importance of compositional tuning in optimizing the efficiency of $CuInS_2$-based solar cells.[52] Doping with elements like Al, Zn, Ag, or Y has also controlled defects, showing improvements in PV charge transfer.[131,139,150,155]

Heterogeneous atom incorporation has also become quite popular in $CuInX_2$ devices due to its ability to modify the

electronic and optical properties, thereby facilitating charge separation, collection, and injection.[148] Some examples of alkaline doping include Mg doping of $CuInS_2$ at different concentrations (0, 2, 4, 8, 10 μmol). This doping modified the absorption spectra, showing a broader range toward the visible region. The band gap was reduced from 1.81 eV (undoped $CuInS_2$) to 1.53 eV at 8 μmol. This concentration also gave the highest increase in V_{oc} and J_{sc}, leading to a PCE of 6.28% compared to 4.83% for the undoped $CuInS_2$. The improvement was explained by a higher rate of electron injection to the TiO_2.

However, higher magnesium concentrations reduced both the absorption capability of the material and the device performance, as seen in Fig. 6e.[148]

Alkaline metals, such as sodium and potassium, have become popular approaches to improve grain boundary quality during the formation process in search of better charge carrier mobilities, as improved performance metrics were achieved by the unexpected diffusion of Na from soda lime glass into the photovoltaic layers.[144] In a study by Chugh *et al.*,[156] simulations of several grain boundaries with structural defects such as voids and dangling bonds were carried out. These were compared to cases with incorporated alkaline metals such as Na, Li, K, and Rb. The study revealed differences in ion diffusion. Metals with a larger ionic radius, like Rb, showed low diffusion rates. In contrast, lighter atoms like Na had higher diffusion rates. However, all ions were found to concentrate in the grain boundaries. It was found that both intrinsic and extrinsic defects (induced by alkaline metals) increase device efficiency by preventing nonradiative recombination from occurring at the grain boundaries.[156] Although alkali metals like Rb[27] and Na have demonstrated beneficial effects in performance metrics, higher concentrations of alkali metals have also been detrimental in film formation by increasing the porosity of the layer.[144] Alkali metals like sodium have also been shown to positively affect the selenization process by forming a Na–Se–O layer, which prevents the formation of surface defect sites like V_{Se}.[144]

Care must be taken when selecting layers from the contact and buffer layers. Layer alignment has been demonstrated to be a key aspect in elevating PCE values. For example, replacing aluminum-doped zinc oxide (AZO) with indium tin oxide IZO as the transparent contact layer TCO front contact in CIS solar cells reduces free-carrier absorption in the NIR, improving current collection. IZO has higher electron mobility (47.3 *vs.* 14.7 $cm^2 V^{-1} s^{-1}$). This change boosts efficiency to 19.2% despite minor losses in the UV range due to IZO's lower bandgap.[27] In another study, the morphological and optoelectronic properties of $CuInSe_2$ films were found to be dependent on the type of TCO used (FTO, FTO/NiO_x, FTO/MoO_3), which affected grain size, band gap, and charge carrier mobility.[157]

Among the different solar cell architectures, tandem solar cells hold the most promise, as the use of different absorber layers can increase the overall PCE through the absorption of multiple regions of the solar spectrum.[158] Among the different combinations, $CuInS_2$ and $CuInSe_2$ have been ideal candidates to support perovskite-based tandem devices as bottom absorbing layers. Examples of these architectures include the work of Jang *et al.*, in which a top layer of perovskite and a bottom layer of $CuInSe_2$ achieved a PCE of 10.3%, obtained through the optimization of parameters such as the thickness of the AZO layer, which played an important role in reducing interfacial resistance. However, device performance was close to standalone $CuInSe_2$, which reached 10.64%. The authors claimed that the reduction in FF in the tandem device could be associated with interfacial resistance and parasitic absorption from the transparent window layers.[159] As a strategy to reduce the parasitic absorption of films like IZO in tandem devices, Jian *et al.* developed a hydrogen-doped In_2O_3 layer through high-vacuum sputtering. The addition of this layer, instead of traditional transparent conductive oxides, helped increase the carrier mobility up to 129 $cm^2 V^{-1} s^{-1}$ and reduced the parasitic absorption above 600 nm caused by the ITO layer. When tested as a perovskite top cell arrangement, the device achieved a PCE of 17.3% while maintaining a transmittance of 82% in the range of 820–1300 nm. The standalone $CuInSe_2$ device reached a PCE of 18.1%, and as a 4-terminal device, the overall PCE increased to 24.6%.[160]

Two-terminal devices have also been improved by combining perovskites and $CuInSe_2$, as shown by Ruiz-Preciado *et al.* In their work, it was discussed that 2-terminal devices with subcells interconnected in series must match their current generation to avoid current limitation by the lowest-producing cell. For that, band gap engineering across the two cells can be done to match the generated photocurrent. Through computational modeling, they determined that the optimal band gap range must lie between 0.95–1.15 eV for the bottom cell and 1.54–1.72 eV for the top cell to achieve PCEs of up to 25%. The bottom cell band gap range can be achieved by using $CuInSe_2$ with low gallium content, which has a band gap of approximately 1.03 eV, while the top perovskite layer should have a band gap around 1.59 eV to reach the desired 25% PCE. Using these parameters, the group produced a 2-terminal device that reached 24.9% PCE measured in-house and a certified efficiency of 23.5%.[158]

Another strategy to increase the PCE is the utilization of reflected light by surfaces interacting with the back of the device. For this, a transparent contact must be added to allow light to enter through the back side. An *et al.* replaced common non-transparent layers like Mo with a transparent conductive oxide such as ITO to fabricate a bifacial transparent $CuInSe_2$ layer. The device performance was further tuned by modifying parameters like the $CuInSe_2$ layer thickness (300–800 nm) and by using NaF for grain boundary passivation and suppression of donor defects like In_{Cu} and V_{Se}. Final evaluation showed that the bifacial $CuInSe_2$ devices achieved PCEs of 6.32% (300 nm) and 10.6% (800 nm). To test albedo conditions, the devices were illuminated from both sides under 2-sun illumination, leading to increased PCEs of 9.41% and 13.9%, respectively. Furthermore, a 4-terminal device was tested by adding a perovskite top cell, achieving PCEs of 18.8% (300 nm) and 21.1% (800 nm) without albedo; under 2-sun conditions, the PCEs rose to 23.4% and 24.4%, respectively.[134]

Other devices have included the use of conductive polymers or organic structures to improve charge carrier transport, such

as liquid crystals, whose molecular arrangement can benefit charge transfer. However, it has been shown by Singh *et al.* that the presence of QDs like $CuInS_2$/ZnS can disturb the structural arrangement of ferroelectric liquid crystals. Despite this, the presence of the liquid crystal in conjunction with the QDs enhances the capacitance of the devices compared to pure ferroelectric liquid crystals.[161] The use of polymeric materials has also helped avoid the need for long capping ligands, as $CuInS_2$ nanocrystals can be fabricated within their structure by thermal decomposition of molecules containing the metal and non-metal precursors. This was demonstrated by Rath *et al.*, who elaborated devices through the decomposition of metal xanthates dissolved into the polymer, which was previously dispersed on the substrate by spin coating, followed by thermal treatment around 195 °C to form the nanocrystals. Further modification with 1,3-benzenedithiol aided surface passivation of the $CuInS_2$ nanocrystals, improving the PCE from 1.87% to 2.56% when 1,3-benzenedithiol was used as the passivating ligand.[162]

The combination of $CuInS_2$ and $CuInSe_2$ with the heavier chalcogenide tellurium (Te) has also gained interest for solar cell applications. Although bulk $CuInTe_2$ has a band gap of 1.02 eV it can be tuned at the quantum dot level through quantum confinement, where the band gap increases as particle size decreases.[18,163] Another strategy to optimize its properties is alloying $CuInTe_2$ with other chalcogenides such as selenium. For example, Kim *et al.* investigated mixed chalcogenide compositions like $CuInTe_{2-x}Se_x$. In their work, quantum dots with a stoichiometry of $Cu_{0.23}In_{0.36}Te_{0.19}Se_{0.22}$ showed greater stability than the Te-only composition ($CuIn_{1.5}Te_{2.5}$). XPS analysis revealed that the Te-only QDs were more susceptible to air oxidation, forming TeO_2 species, while the Se/Te alloyed QDs showed no clear signs of oxidation. When applied in solar cells, the alloyed QDs achieved a PCE (PCE) of 3.1%, with a J_{sc} of 17.4 mA cm^{-2}, a V_{oc} of 0.40 V, and a FF of 44.1% under AM 1.5G illumination at 100 mW cm^{-2}.[164] In another study by Buatong *et al.*, several compositions of $CuInTe_{2-x}Se_x$ quantum dots were tested in dye-sensitized solar cells. The authors observed that the optical absorption properties of the QDs varied depending on the ratio between the chalcogen elements. Specifically, a higher selenium content was associated with an increase in band gap energy. Among the tested stoichiometries, the best photovoltaic performance was achieved using $CuInTe_{1.2}Se_{0.8}$, which yielded the highest PCE (3.751%) under standard 1 sun illumination.[163] Even though experimental studies have addressed the impact of chalcogen mixtures with tellurium, $CuInTe_2$ holds promise as an efficient solar absorber. Computational studies indicate that a PCE of 24.21% can be achieved with a n-CdS/p-$CuInTe_2$ single-junction solar cell with proper optimization. Furthermore, the efficiency can be elevated up to 34.32% with the introduction of a MoS_2 back surface field layer.[165]

6.1.1. Device stability. In solar cell devices, ternary chalcogenides can undergo several degradation pathways depending on the type of physical or chemical stress and the surrounding chemical environment, especially at interfaces. As shown by Colombara *et al.*, the stoichiometry of $CuInS_2$ plays a key role in its degradation behavior. $CuInS_2$ absorber devices were found to be susceptible to oxygen. The rate of degradation was dependent on stoichiometry: copper-rich compositions were more prone to oxidation of selenide anions under ambient conditions, leading to the formation of In_2O_3 and Cu_2Se phases. This, in turn, induced the formation of anion vacancies, which negatively impacted device performance. It was also found that using KCN to remove Cu_2Se phases caused leaching of both Se and Cu, leading to defect formation related to Se vacancies. The density of these defects was higher in copper-rich compositions, resulting in a reduced V_{oc}. The involvement of selenium-related defects was confirmed by post-deposition treatments using different Se-containing species, which led to improvements in V_{oc}. Interestingly, it was observed that after KCN treatment and the formation of Se-related vacancies, further oxygen exposure appeared to passivate these defects, improving the photocurrent density.[141] Similarly, Elizabeth *et al.* also detected the presence of In_2O_3 and SeO_x signals through XPS after air oxidation of $CuInSe_2$. Further treatment with KCN was able to remove traces of SeO_x, although In_2O_3 persisted and could only be eliminated by a subsequent annealing treatment under ultra-high vacuum.[166]

Apart from surface oxidation, cation mobility is a concern in $CuInS_2$ and $CuInSe_2$ solar cells, as cations can segregate within the structure. In memristor devices, it has been observed that under an external electric potential, Cu atoms can oxidize to Cu^{2+} and migrate into cathodes such as ITO, causing copper accumulation at the interface between the two layers. This mobility increases with the strength of the electric field.[167] To our knowledge, no migration of Cu has been reported toward interfaces like TiO_2 in sensitized solar cells, likely because the electric fields involved are much weaker than those in memristors. However, copper diffusion has been observed in $CuInS_2$/In_2S_3 solar cells when $CuInS_2$ is deposited through spray pyrolysis, negatively affecting the device performance. This issue has been addressed by depositing a double layer of $CuInS_2$ with different stoichiometries, copper-rich near the electrode and copper-poor at the junction region, effectively reducing Cu diffusion and improving device stability.[168]

6.2. Luminescent solar concentrator (LSC)

Compared to solar cells, where materials like $CuInX_2$ are tasked with absorbing light and subsequently separating charges for direct energy conversion, in LSCs, $CuInX_2$ materials act as fluorophores that capture light and re-emit it at different wavelengths. The emitted light is then redirected into the attached solar cells with minimal energy loss.[51,169,170] In this context, key aspects regarding the material's optical properties and interface engineering are crucial for achieving device construction with high PCE. First, a key property of the fluorophore is a significant Stokes shift, which relates to the distance between the absorption peak of the molecule and the emission wavelength. A greater Stokes shift prevents reabsorption losses ascribed to emission and absorption band overlap.[51] The absence of these stoke shifts present a significant challenge for LSC materials such as organic fluorophores. Although such molecules are inexpensive, their slight Stokes.

Another critical issue is the durability of fluorophores; multiple studies have shown the efficiency of a variety of fluorophores albeit they often rely on short-term exposures. In a 3-year study, Terricabres-Polo *et al.*[90] tested the performance of multiple device compositions, including $CuInS_2$/ZnS, InP/ZnSe/ZnS, CdSe/CdS/ZnS core–shell QDs (QDs), and Lumogen, a widely studied organic luminophore (Fig. 7a).[90] Among all the devices, $CuInS_2$/ZnS outperformed the others in terms of optical properties, device performance, and stability, exhibiting the broadest absorption spectrum, an absorption of 28% of the incoming light flux, and the highest median PCE over three years (Fig. 7a).[90] Over the duration of the study, devices based on $CuInS_2$ and InP showed improved performance and durability. This was attributed to the polymer, which effectively protected both $CuInS_2$ and InP devices, maintaining their stability for up to two years.[90] However, $CuInS_2$ demonstrated better resistance to outdoor conditions than InP. This was linked to differences in their charge recombination dynamics. $CuInS_2$ benefits from a localized hole and a delocalized electron, making it less prone to PL quenching caused by hole traps. In contrast, InP, with localized electrons and holes, was more susceptible to such quenching.[90]

$CuInX_2$ materials show a large enough Stokes shift to attract interest in this field.[169] However, their typically low QY values limit direct applications. A key challenge, which has seen progress over the years, is improving the QY, as strong emission is needed for high PCE. Doping, alloying, or coreshelling with materials like ZnS is often used to enhance the PL properties of $CuInX_2$. Although these strategies increase QY, they can cause a blue Stokes shift, increasing overlap between emission and

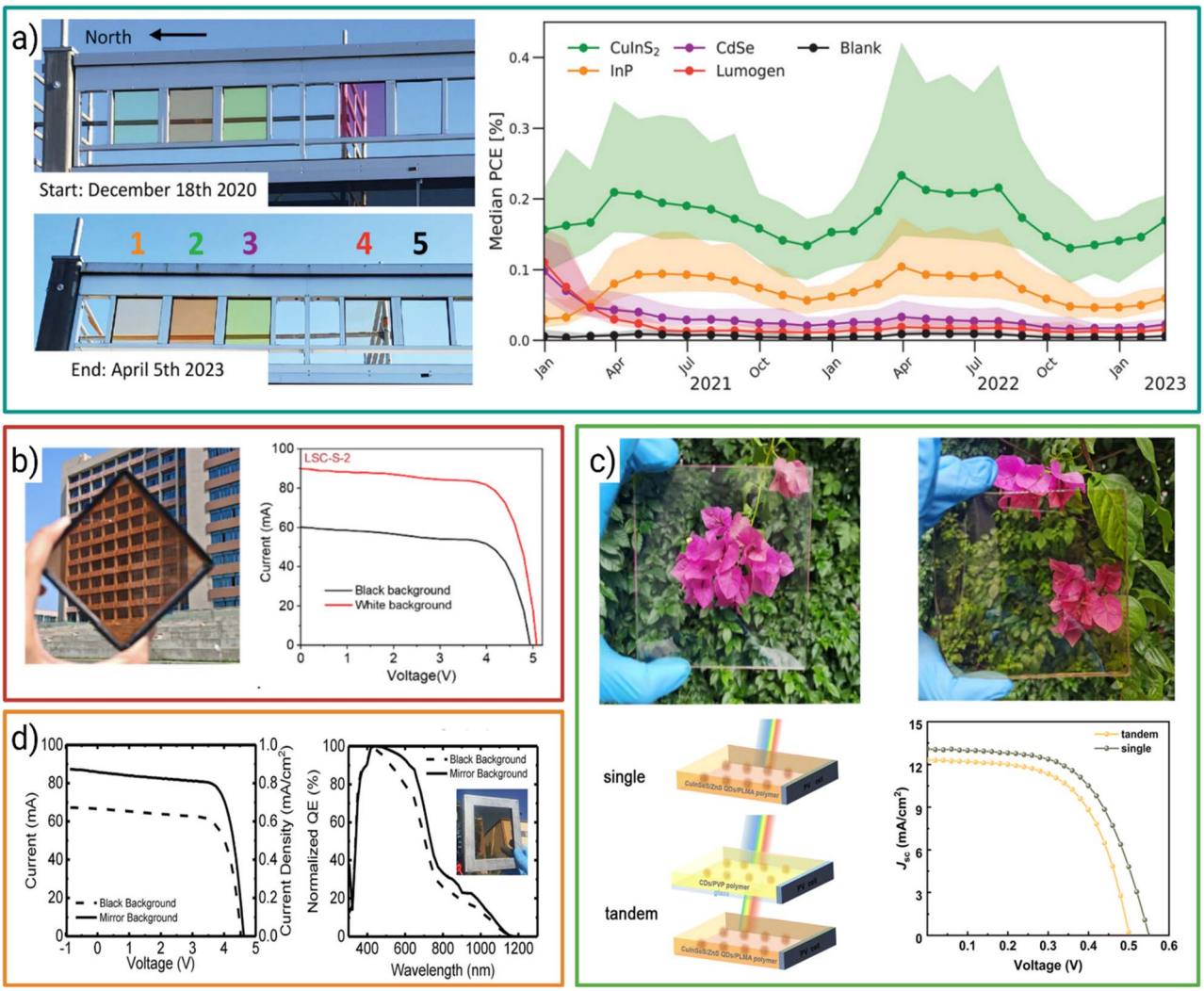

Fig. 7 (a) Multiple LSC devices fabricated with InP/ZnSe/ZnS QDs (1), $CuInS_2$/ZnS QDs (2), CdSe/CdS/ZnS QDs and (3), Lumogen Red F305 (4) and blank LSCs (5), with their respective median power conversion efficiency over 3 years, adapted with permission from ref. 88. Copyright 2024, Wiley-VCH. (b) $CuInS_2$/ZnS luminescent solar concentrator fabricated with thiol-ene polymers and its *I*–*V* curves with black and white backgrounds, adapted with permission from ref. 48. Copyright 2024 The Royal Society of Chemistry. (c) LSCs based on carbon dots and $CuInS_2$/ZnS QDs, evaluation of *I*–*V* curves as single and tandem devices, adapted with permission from ref. 31. Copyright 2024 The Royal Society of Chemistry. (d) NREL certified *I*–*V* for a $CuInS_2$/ZnS LSCs with black and mirrored background, along with averaged quantum efficiency from four locations with black and mirrored background, adapted with permission from ref. 32. Copyright 2018 American Chemical Society.

Table 3 Summary of $CuInS_2$ and $CuInSe_2$ based photovoltaic devices, including device architectures, deposition methods, and corresponding performance metrics

Material	Architecture	Deposition	PCE	V_{oc}	J_{sc}	FF	Ref.
$CuInSe_2$ doped with Mg	FTO/TiO_2/CISe or MnCISe/polysulfide electrolyte/Cu_2S/FTO	Adsorption on TiO_2	6.28	687 mV	18.11	50.5	148
$CuInS_2$	ITO/PEDOT:PSS/PCDTBT:$CuInS_2$/Ag	Spin coating	0.21	0.716 mV	1.09	0.27	106
$CuInS_2$	Mo-SLG/$CuIn(S, Se)_2$/CdS/i-ZnO/ITO/Ni/Al/MgF_2	Precursor annealing on Mo-coated soda lime glass	9.46	0.45 V	35.04	59.93	149
Zn:$CuInSe_2$	FTO/TiO_2/$CuInSe_2$/ZnS/polysulfide electrolyte/brass or mesoporous carbon	Deep coating	9.4	603	26.5	59.3	72
Al/Zn $CuInSe_2$	FTO/TiO_2 + QDs/ZnS/polysulfide electrolyte/Cu_2S on brass	Adsorption of TiO_2 films	10.18	0.622 V	27.13	60.3	150
$CuInS_2$	Mo/CIS/CdS/i-ZnO/IZO/Ni/Al + MgF_2	Co-evaporation	18.1	0.590 V	41.8	73.2	132
$CuInSe_2$	ITO/CISe QD/perovskite/PCBM, BCP/Ag	Spin coating	8.59	0.80	16.3	59.3	25
$CuInS_2$	Au/CIS QDs/perovskite + TiO_2/FTO	Spin coating	12.33	864 mV	21.69	66	135
$CuInSe_2$	ITO/SnO_2/$MAPbI_3$ + $CuInSe_2$ QDs/spiro-OMeTAD/Ag	Spin coating	18.041	1.093 V	21.086	78.35	133
$CuInSe_2$	ITO/SnO_2/$CsPbI_{1.2}Br_{1.8}$ perovskite with CISe QDs/spiro-OMeTAD/Au	Spin coating	10.26	1.28 V	11.54	69.40	151
$CuInSe_2$	ITO/$CuInSe_2$/CdS/i-ZnO/IZO	Co-evaporation	10.6	0.454 V	33.5	69.8	134
$CuInSe_2$	SLG/Mo/CISe/CdS/i-ZnO/n-ZnO/Al	Spin coating	12.83	0.491 V	38.59	67.74	144
$CuInSe_2$	Si_3N_4/Mo/CISSe/CdS/i-ZnO/Al:ZnO/Ni:Al	Spin coating	9.6	464.5 mV	33.4	62	152
$CuInS_2$	Glass/ITO/PEDOT:PSS/PCDTBT:$CuInS_2$/Ag	Spin coating	0.23	0.73	1.16	27.2	106

absorption spectra and reducing device efficiency.[30,36] To address this, surface engineering and coupling with a polymer matrix have been explored to enhance the Stokes shift.[51] In the work of Wu *et al.*, thiol-containing monomers were used to create off-stoichiometric thiol-ene polymers.[51] Possessing a high affinity for cations like Cu or Zn, the interactions coming from the thiol groups caused an increment in the Stokes shift of 151 meV, which was attributed to the modification of Cu^+ defect energy states due to the electron-donating ability of thiol groups.[51] This interaction also prevented the reduction in QY, as observed in non-thiol-containing polymers like PLMA and PMMA.[51] The enlargement of the Stokes shift contributed to an increase in the PCE of the device, achieving a certified efficiency of 1.36% for medium-area (9 × 9 cm^2) LSCs (Fig. 7b). In comparison, large-area LSCs (29 × 29 cm^2) achieved 4.25%.[51]

Apart from designing fluorophores with near-unity QY and sufficiently large Stokes shifts to avoid reabsorption losses, the dispersibility of QDs in the polymer matrix plays a substantial role in defining the optical properties related to light transmission.[89] Multiple studies have demonstrated the role of surface ligands and structure matching with the polymer matrix in determining transmittance, waveguiding, and refractive index matching.[89] Common issues related to haze, which results in non-transparent polymer nanocomposites, can be solved by a better selection of the polymer matrix associated with the structure of the ligand on the surface of the QDs. However, some strategies can involve ligand exchange to more suitable structures compatible with the most common polymers, such as polymethyl methacrylate (PMMA), polycarbonate (PC), epoxy, polystyrene (PS), polyethylene (PE), polypropylene (PP), and polyethylene terephthalate (PET). The incompatibility of surface ligands further limits the application of $CuInX_2$ in advanced polymers, such as UV-curable celloxides. For example, $CuInS_2$/ZnS covered by hydrophilic ligands like MPA resulted in lower transmittance and more significant aggregation than cyclohexyl 3-mercaptopropionate.[89] The latter was carefully selected due to its structural similarity to celloxides, which led to higher transmittance, reduced haze, and improved QY in the polymer, as opposed to the MPA-coated QDs.[89]

Although haze is generally avoided in the luminophore layer of an LSC, it can be beneficial when incorporated into other layers. Advanced technologies, such as thermally responsive materials, can alter the transmittance of the LSC by incorporating optical scattering to redirect light back into the luminophore layer, thereby increasing device efficiency. Chen *et al.*[91] tested such an architecture, utilizing a thermally responsive layer composed of polydimethylsiloxane (PDMS) and an ethylene glycol solution. This layer demonstrated the ability to change the device's transmittance across a temperature range of 20–50 °C. At ambient temperatures (25 °C), the visible light transmittance (VLT) was 83.5%, which decreased to 56.5% at 50 °C. The enhanced light scattering at higher temperatures had a positive impact on the PCE, increasing from 1.21% at 25 °C to 1.36% at 50 °C.[91]

Although previous research has demonstrated that $CuInS_2$ materials exhibit a high degree of stability, as shown by Wang *et al.*, they still suffer from PLQY reductions due to environmental factors such as UV exposure,[30] where a single layer device of $CuInS_2$/ZnS had a 21% decrease of PL intensity after 8 hours of irradiation under a 395 nm, 50 W lamp.[30] As shown by Wang *et al.*, other protective and emissive materials can be added to serve as LSC devices to address issues such as photobleaching,[30] where a tandem device architecture consisting of a layer of $CuIn(Se,S)_2$/ZnS QDs and a layer of carbon dots (CDs) (Fig. 7c) was used.[30] Although the PCE in the tandem devices was not greater than that of the single-layer device, the optical stability was improved, maintaining a 93% PL intensity compared to a 21% loss by the single-layer device.[30]

Table 4 Photophysical and photovoltaic properties of $CuInS_2$-based coreshell quantum dots, including absorption range (AR), emission (Em), stokes shift (SS), quantum yield, LSC device size, power conversion efficiency (PCE), optical efficiency (OE), solar absorption (SA), and encapsulation materials

Fluorophore	AR (nm)	Em (nm)	SS (meV)	QY (%)	Size	PCE (%)	OE	SA	Encapsulation	Ref.
$CuInS_2$/ZnS	300–600	550	—	81%	—	8.71	—	—	PMMA	32
$CuInS_2$/CdS	400–700	~740	—	75% in toluene	—	5.7	—	—	PLMA	171
$CuInS_2$/ZnS	300–800	862	>550	91% in nonpolar solvent	10 × 10 cm	2.94[a] 2.18[b]	8.1	35.5	PLMA	31
$CuInS_2/ZnSe_xS_{1-x}$	300–600	~600	—	13–70 depending on the shell Se:S composition in the solution 9.3–65% in solid	10 × 10 cm	0.53	—	—	PVP	82
$CuInS_2$/ZnS	300–800	830	—	—	15.24 cm × 15.24 cm	3.6[a]	—	57.2[a]	—	172
Tandem LSC (CDs + $CuInSe_{2-x}S_x$/ZnS	300–800	878 (CuInSeS/ZnS)	580 (CDs), 530 (CuInSeS/ZnS)	61%)	10 × 10 × 0.3 cm^3	0.46 (tandem), 0.50 (single-layer CuInSeS/ZnS)	—	—	PVP and PLMA-*co*-EGDM	30
CuIn(S, $Se)_2$/ZnS	300–1000	833–1088	~519	45–83%	5 × 5 × 0.9 cm^3	1.19–1.36	—	—	PDMS	91
$CuInS_2$/ZnS	400–700	~500 nm in OSTE	585 in OSTE	85 in OSTE	—	1.36	—	—	Off stoichiometric thiolene	51

[a] With reflective substrate. [b] With no reflective substrate. Polymethyl methacrylate (PMMA), poly(lauryl methacrylate-*co*-ethylene glycol) (PLMA), polyvinylpyrrolidone (PVP), poly(lauryl methacrylate) (PLMA), ethylene glycol dimethacrylate (EGDM), polydimethylsiloxane (PDMS).

In tandem devices, each QD layer with a different band gap is designed to absorb a specific part of the solar spectrum, allowing for its further emission and absorption by the PV device. If the QD layers share the same type of PV device, energy losses can occur as a consequence of a mismatch between the QD emission and the PV band gap. This was noted by Wu *et al.*[169] who used computational modelling to show that PV band gap matching in a QD tandem device can lead to an improvement from 3.1 to 3.8% when an appropriate PV device is selected for each layer.[169]

In another study, Bergren *et al.*[31] synthesized QDs of $CuInS_2$/ZnS with a Stokes shift >550 meV and a QY of 91% in non-polar solvents. However, the QY decreased to 66% when the dots were encapsulated in a polymer matrix. These QDs were used to create a nanocomposite sandwiched between two pieces of low-iron-content glass, which acted as a waveguide and reduced the polymer's optical losses and optical requirements.[31] The device demonstrated a visible light transmittance of 43.7% and solar absorption of 35.5%. Performance testing, as shown in Fig. 7d, revealed a PCE of 2.18% for a non-reflective substrate and 2.94% when using a reflective counterpart, indicating that the device was capable of producing between 22 and 30 W m^{-2} under certain specifications.[31] Additionally, an averaged quantum efficiency was measured from four locations, comparing reflective and non-reflective substrates. Bergren *et al.*[31] discussed strategies to enhance the PCE further to achieve a benchmark of 50 W m^{-2}, including optimizing the form factor of the embedded solar cell, increasing its intrinsic efficiency, reducing haze, and improving sunlight absorption.[31] Their model suggested that surpassing the energy generation benchmark of 50 W m^{-2} would render these devices suitable for tall buildings. For an 80-story building, such performance could yield approximately 1 GWh of electricity annually, translating to an estimated economic benefit of around $200 000.[31] Table 3 presents other works related to LSC and their achieved performance metrics.

7. Conclusions

As discussed throughout this review, ternary copper chalcogenides, such as $CuInX_2$ (X = S, Se), are a unique class of materials well-suited for solar energy conversion They offer broad optical tunability through multiple parameters, including quantum dot size, metal composition, and chalcogenide ratio, while presenting lower toxicity than many binary chalcogenides that often contain heavy metals, this has helped to develop devices capable of absorbing lower energy wavelengths that other binary phases or materials like perovskite have been uncapable to take advantage. However, a deeper understanding of their intrinsic properties is still required to enable their efficient integration into devices such as solar cells and luminescent solar concentrators. In particular, they currently lack key advantages found in binary chalcogenides, such as precise control over composition and size distribution, both of which are essential for achieving high power conversion efficiencies (PCEs). Among the key challenges involved in the ternary chalcogenide research, we believe the following aspects are key to advancing their development:

Recent studies suggest that the photoluminescence mechanism involves a free-to-bound donor–acceptor pair, often linked to Cu^{+} or Cu^{2+} states, whose distribution depends on the sample's stoichiometry. Fully understanding the location and nature of these traps is essential for controlling PL behavior, improving QY without the need for surface passivation, and suppressing non-radiative recombination – two factors that are known to be critical for boosting device PCE. This knowledge can also guide stoichiometry control to selectively favor defects that are either beneficial for solar cells or LSCs.

As discussed in the synthesis section, sulfur-based nanomaterials benefit from readily available and easy-to-handle precursors, such as DDT. In contrast, selenium-based compositions still rely on toxic precursors or complex ligand combinations, including DDT to produce colloidally compatible selenium sources. This often prevents the formation of pure-phase $CuInSe_2$. Designing selenium precursors that are both safe and compatible with colloidal synthesis is crucial for enabling the fabrication of phase-pure $CuInSe_2$ nanomaterials. This is especially important for applications that require the specific optical properties of the pure selenide phase. This could also benefit the stoichiometric and size control of the selenide compositions, as it wouldn't involve the formation of sulfur-related phases.

Regarding solar cells, interfacial layer treatments have recently proven effective in increasing device efficiency. Therefore, more attention should be given to passivating these interfaces to reduce unwanted recombination and prevent energy losses.

In the case of LSCs, copper chalcogenides have proven to be efficient due to their large Stokes shifts and potential for high QY, often improved through passivation strategies, such as ZnS core–shell structures. However, efforts should be made to avoid the blueshift in emission that occurs as a result of these treatments. Minimizing this shift is crucial to reducing reabsorption losses and enhancing overall device performance.

Progress in the aspects mentioned above will help to establish ternary copper chalcogenides as key materials for the next generation of efficient, low-cost, and sustainable solar energy conversion devices.

Conflicts of interest

There are no conflicts to declare.

Data availability

No primary research results, software or code have been included and no new data were generated or analysed as part of this review.

Acknowledgements

R. N. acknowledges financial support from the Natural Sciences and Engineering Research Council (NSERC) through the Discovery Grant Program, as well as from Concordia University (Montreal, Canada) *via* the Research Chair Program. Additional funding was provided by the Quebec Centre for Advanced Materials. L. P. is grateful for funding provided by the Fonds de recherche du Québec Nature et technologies (FRQNT) (**https://doi.org/10.69777/366779**) through the Doctoral Research Scholarship, and by the Secretariat of Science and Technology (SEHCITI, Mexico) through the Doctoral Studies Abroad Scholarship. M. D. acknowledges support from the FRQNT through the Doctoral Research Scholarship (**https://doi.org/10.69777/344576**). G. F. is grateful for funding provided by the Natural Sciences and Engineering Research Council of Canada (NSERC) through the Canada Graduate Scholarships Master's (CGSM) program, as well as by the FRQNT through the Master's research grants (**https://doi.org/10.69777/342339**). D. P. S. and R. N. are thankful to the France-Quebec scientific cooperation by Consulat général de France à Québec for financing the Samuel de Champlain project (0185-CAN-22-0010).

References

1 S. Nanda and A. K. Dalai, *Biomass to Bioenergy – Modern Technological Strategies for Biorefineries*, Woodhead Publishing, 2024, vol. 7.
2 IEA, *World Energy Outlook 2024*, Paris, 2024.
3 EI - Energy Institute, *Statistical Review of World Energy*, 2024.
4 IEA, Renewables 2024, *Analysis and Forecast to 2030*, Paris, 2024.
5 X. Zhang, Y. Zeng, T. Yu, J. Chen, G. Yang and Y. Li, *J. Phys. Chem. Lett.*, 2014, **5**, 2340–2350.
6 A. H. Munshi, N. Sasidharan, S. Pinkayan, K. L. Barth, W. S. Sampath and W. Ongsakul, *Sol. Energy*, 2018, **173**, 511–516.
7 Z. R. Abdulghani, A. S. Najm, A. M. Holi, A. A. Al-Zahrani, K. S. Al-Zahrani and H. Moria, *Sci. Rep.*, 2022, **12**, 8099.
8 M. B. Hayat, D. Ali, K. C. Monyake, L. Alagha and N. Ahmed, *Int. J. Energy Res.*, 2019, **43**, 1049–1067.
9 C. B. Isabela, R. A. Marques Lameirinhas, J. P. N. Torres and C. A. F. Fernandes, *Sustainable Energy Fuels*, 2021, **5**, 2273–2283.
10 C. B. Isabela, R. A. Marques Lameirinhas, J. P. João and C. A. F. Fernandes, *Sustainable Energy Fuels*, 2021, **5**, 2273–2283.
11 F. Rehman, I. H. Syed, S. Khanam, S. Ijaz, H. Mehmood, M. Zubair, Y. Massoud and M. Q. Mehmood, *Energy Adv.*, 2023, **2**, 1239–1262.
12 V. T. Chebrolu and H. J. Kim, *J. Mater. Chem. C*, 2019, **7**, 4911–4933.
13 S. Chen, B. Zu and L. Wu, *ACS Omega*, 2024, **9**, 43288–43301.
14 D. Sharma, R. Jha and S. Kumar, *Sol. Energy Mater. Sol. Cells*, 2016, **155**, 294–322.
15 M. Sandroni, K. D. Wegner, D. Aldakov and P. Reiss, *ACS Energy Lett.*, 2017, **2**, 1076–1088.
16 S. Liu and X. Su, *RSC Adv.*, 2014, **4**, 43415–43428.
17 E. A. Hernández-Pagán, A. D. P. Leach, J. M. Rhodes, S. Sarkar and J. E. Macdonald, *Chem. Mater.*, 2015, **27**, 7969–7976.
18 C. Coughlan, M. Ibáñez, O. Dobrozhan, A. Singh, A. Cabot and K. M. Ryan, *Chem. Rev.*, 2017, **117**, 5865–6109.

19 A. D. P. Leach and J. E. Macdonald, *J. Phys. Chem. Lett.*, 2016, **7**, 572–583.
20 P. Reiss, M. Carrière, C. Lincheneau, L. Vaure and S. Tamang, *Chem. Rev.*, 2016, **116**, 10731–10819.
21 J. J. Plata, V. Posligua, A. M. Márquez, J. Fernandez Sanz and R. Grau-Crespo, *Chem. Mater.*, 2022, **34**, 2833–2841.
22 A. C. Berends, M. J. J. Mangnus, C. Xia, F. T. Rabouw and C. de Mello Donega, *J. Phys. Chem. Lett.*, 2019, **10**, 1600–1616.
23 J. Huang, M. G. Gatty, B. Xu, P. B. Pati, A. S. Etman, L. Tian, J. Sun, L. Hammarström and H. Tian, *Dalton Trans.*, 2018, **47**, 10775–10783.
24 B. Chen, W. Zheng, F. Chun, X. Xu, Q. Zhao and F. Wang, *Chem. Soc. Rev.*, 2023, **52**, 8374–8409.
25 Y. Zhang, Z. Zhang, Y. Liu, H. Gao and Y. Mao, *Mater. Sci. Semicond. Process.*, 2020, **120**, 105267.
26 D. Deng, Y. Chen, J. Cao, J. Tian, Z. Qian, S. Achilefu and Y. Gu, *Chem. Mater.*, 2012, **24**, 3029–3037.
27 T. Feurer, R. Carron, G. Torres Sevilla, F. Fu, S. Pisoni, Y. E. Romanyuk, S. Buecheler and A. N. Tiwari, *Adv. Energy Mater.*, 2019, **9**, 1901428.
28 L. Zheng, Y. Xu, Y. Song, C. Wu, M. Zhang and Y. Xie, *Inorg. Chem.*, 2009, **48**, 4003–4009.
29 L. J. Lim, X. Zhao and Z.-K. Tan, *Adv. Mater.*, 2023, **35**, 2301887.
30 L. Wang, Y. Chen, Y. Lai, X. Zhao, K. Zheng, R. Wang and Y. Zhou, *Nanoscale*, 2023, **16**, 188–194.
31 M. R. Bergren, N. S. Makarov, K. Ramasamy, A. Jackson, R. Guglielmetti and H. McDaniel, *ACS Energy Lett.*, 2018, **3**, 520–525.
32 C. Li, W. Chen, D. Wu, D. Quan, Z. Zhou, J. Hao, J. Qin, Y. Li, Z. He and K. Wang, *Sci. Rep.*, 2015, **5**, 17777.
33 A. S. Fuhr, H. J. Yun, N. S. Makarov, H. Li, H. McDaniel and V. I. Klimov, *ACS Photonics*, 2017, **4**, 2425–2435.
34 H. J. Yun, J. Lim, A. S. Fuhr, N. S. Makarov, S. Keene, M. Law, J. M. Pietryga and V. I. Klimov, *ACS Nano*, 2018, **12**, 12587–12596.
35 J. W. Turnley, S. D. Deshmukh, V. M. Boulos, R. G. Ellis, N. J. LiBretto, J. K. Y. Liu, J. T. Miller, H. I. Kenttämaa and R. Agrawal, *ACS Omega*, 2023, **8**, 47262–47270.
36 Z. Liu, C. Hao, Y. Sun, J. Wang, L. Dube, M. Chen, W. Dang, J. Hu, X. Li and O. Chen, *Nano Lett.*, 2024, **24**, 5342–5350.
37 Y. H. Jang, J. M. Lee, J. W. Seo, I. Kim and D.-K. Lee, *J. Mater. Chem. A*, 2017, **5**, 19439–19446.
38 J. Ning, Y. Xiong, F. Huang, Z. Duan, S. V. Kershaw and A. L. Rogach, *Chem. Mater.*, 2020, **32**, 7842–7849.
39 A. S. Portniagin, A. A. Sergeev, K. A. Sergeeva, S. Wang, Z. Li, J. Ning, C. C. S. Chan, S. V. Kershaw, X. Zhong, K. S. Wong and A. L. Rogach, *Adv. Funct. Mater.*, 2024, **34**, 2400942.
40 E. Cassette, T. Pons, C. Bouet, M. Helle, L. Bezdetnaya, F. Marchal and B. Dubertret, *Chem. Mater.*, 2010, **22**, 6117–6124.
41 B. Zu, S. Chen, Q. Jin, Z. Xu, X. Wu and L. Wu, *Inorg. Chem.*, 2024, **63**, 21816–21821.
42 A. Richardson, J. Alster, P. Khoroshyy, J. Psencik, J. Valenta, R. Tuma and K. Critchley, *ACS Omega*, 2024, **9**, 17114–17124.
43 P. Joshi, M. Duda, K. Sobczak, R. Minikayev and Ł. Kłopotowski, *J. Phys. Chem. C*, 2023, **127**, 21261–21270.
44 S. M. Harvey, D. W. Houck, W. Liu, Y. Liu, D. J. Gosztola, B. A. Korgel, M. R. Wasielewski and R. D. Schaller, *ACS Nano*, 2021, **15**, 19588–19599.
45 S. M. Harvey, D. W. Houck, M. S. Kirschner, N. C. Flanders, A. Brumberg, A. A. Leonard, N. E. Watkins, L. X. Chen, W. R. Dichtel and X. Zhang, *ACS Nano*, 2020, **14**, 13548–13556.
46 D. W. Houck, E. I. Assaf, H. Shin, R. M. Greene, D. R. Pernik and B. A. Korgel, *J. Phys. Chem. C*, 2019, **123**, 9544–9551.
47 A. T. Nguyen, F. Gao, D. Baucom and C. D. Heyes, *J. Phys. Chem. C*, 2020, **124**, 10744–10754.
48 K. Qi, Y. Wang, R. Wang, D. Wu and G.-D. Li, *J. Mater. Chem. C*, 2016, **4**, 1895–1899.
49 B. Pejova, E. Sherif and M. W. Minde, *J. Phys. Chem. C*, 2020, **124**, 20240–20255.
50 Y. Wang, X. Zhao, F. Liu, X. Zhang, H. Chen, F. Bao and X. Liu, *RSC Adv.*, 2014, **4**, 16022–16026.
51 Y. Wu, J. Huang, J. Zang, J. Zhou, C. Cheng, Z. Hu, D. Shan, W. Yang, I. Sychugov, L. Sun and B. Xu, *Energy Environ. Sci.*, 2024, **17**, 6338–6349.
52 G. Wang, H. Wei, J. Shi, Y. Xu, H. Wu, Y. Luo, D. Li and Q. Meng, *Nano Energy*, 2017, **35**, 17–25.
53 Y. Nakamura, Y. Iso and T. Isobe, *ACS Appl. Nano Mater.*, 2020, **3**, 3417–3426.
54 S. Qu, X. Yuan, Y. Li, X. Li, X. Zhou, X. Xue, K. Zhang, J. Xu and C. Yuan, *Nanoscale Adv.*, 2021, **3**, 2334–2342.
55 H. Zhong, S. S. Lo, T. Mirkovic, Y. Li, Y. Ding, Y. Li and G. D. Scholes, *ACS Nano*, 2010, **4**, 5253–5262.
56 C. Xia, W. Wu, T. Yu, X. Xie, C. van Oversteeg, H. C. Gerritsen and C. de Mello Donega, *ACS Nano*, 2018, **12**, 8350–8361.
57 J. Chen, L. Zhang, S. Li, F.-L. Jiang, P. Jiang and Y. Liu, *ACS Appl. Nano Mater.*, 2021, **4**, 6057–6066.
58 O. Yarema, D. Bozyigit, I. Rousseau, L. Nowack, M. Yarema, W. Heiss and V. Wood, *Chem. Mater.*, 2013, **25**, 3753–3757.
59 F. Liu, J. Zhu, Y. Xu, L. Zhou and S. Dai, *Nanoscale*, 2016, **8**, 10021–10025.
60 S. Deka, A. Genovese, Y. Zhang, K. Miszta, G. Bertoni, R. Krahne, C. Giannini and L. Manna, *J. Am. Chem. Soc.*, 2010, **132**, 8912–8914.
61 E. Dilena, Y. Xie, R. Brescia, M. Prato, L. Maserati, R. Krahne, A. Paolella, G. Bertoni, M. Povia, I. Moreels and L. Manna, *Chem. Mater.*, 2013, **25**, 3180–3187.
62 N. J. Simi, L. Kuriakose, R. Vinayakan and V. V. Ison, *RSC Adv.*, 2018, **8**, 37146–37150.
63 D. Yao, H. Liu, Y. Liu, C. Dong, K. Zhang, Y. Sheng, J. Cui, H. Zhang and B. Yang, *Nanoscale*, 2015, **7**, 18570–18578.
64 J.-J. Wang, P. Liu and K. M. Ryan, *Chem. Commun.*, 2015, **51**, 13810–13813.
65 J. Li, M. Bloemen, J. Parisi and J. Kolny-Olesiak, *ACS Appl. Mater. Interfaces*, 2014, **6**, 20535–20543.
66 H. Reinhold, U. Mikolajczak, I. Brand, C. Dosche, H. Borchert, J. Parisi and D. Scheunemann, *J. Phys. Chem. C*, 2020, **124**, 19922–19928.

67 K. Wang, Z. Liang, J. Li, X. Xu, X. Cheng, H. Jin, D. Xu and G. Xu, *J. Mater. Sci.*, 2019, **54**, 2037–2048.
68 H. Wang, J. Hu, M. Zhu, Y. Li, H. Qian, X. Shen, F. Liebner and T. Rosenau, *RSC Adv.*, 2019, **9**, 25576–25582.
69 J. Ning, Z. Duan, S. V. Kershaw and A. L. Rogach, *ACS Nano*, 2020, **14**, 11799–11808.
70 M. Gromova, A. Lefrançois, L. Vaure, F. Agnese, D. Aldakov, A. Maurice, D. Djurado, C. Lebrun, A. de Geyer, T. U. Schülli, S. Pouget and P. Reiss, *J. Am. Chem. Soc.*, 2017, **139**, 15748–15759.
71 Z. Wang, X. Zhang, W. Xin, D. Yao, Y. Liu, L. Zhang, W. Liu, W. Zhang, W. Zheng, B. Yang and H. Zhang, *Chem. Mater.*, 2018, **30**, 8939–8947.
72 J. Du, R. Singh, I. Fedin, A. S. Fuhr and V. I. Klimov, *Nat. Energy*, 2020, **5**, 409–417.
73 A. C. Berends, F. T. Rabouw, F. C. M. Spoor, E. Bladt, F. C. Grozema, A. J. Houtepen, L. D. A. Siebbeles and C. De Mello Donegá, *J. Phys. Chem. Lett.*, 2016, **7**, 3503–3509.
74 H. D. Nelson and D. R. Gamelin, *J. Phys. Chem. C*, 2018, **122**, 18124–18133.
75 W. Van Der Stam, M. De Graaf, S. Gudjonsdottir, J. J. Geuchies, J. J. Dijkema, N. Kirkwood, W. H. Evers, A. Longo and A. J. Houtepen, *ACS Nano*, 2018, **12**, 11244–11253.
76 A. Fuhr, H. J. Yun, S. A. Crooker and V. I. Klimov, *ACS Nano*, 2020, **14**, 2212–2223.
77 S. O. M. Hinterding, M. J. J. Mangnus, P. T. Prins, H. J. Jöbsis, S. Busatto, D. Vanmaekelbergh, C. de Mello Donega and F. T. Rabouw, *Nano Lett.*, 2021, **21**, 658–665.
78 C. Xia, P. Tamarat, L. Hou, S. Busatto, J. D. Meeldijk, C. De Mello Donega and B. Lounis, *ACS Nano*, 2021, **15**, 17573–17581.
79 A. Harchol, Y. Barak, K. E. Hughes, K. H. Hartstein, H. J. Jöbsis, P. T. Prins, C. De Mello Donegá, D. R. Gamelin and E. Lifshitz, *ACS Nano*, 2022, **16**, 12866–12877.
80 M. Szymura, M. Duda, M. Karpińska, T. Kazimierczuk, R. Minikayev, K. Sobczak, M. Parlińska-Wojtan and Ł. Kłopotowski, *J. Phys. Chem. C*, 2023, **127**, 6768–6776.
81 A. C. Berends, W. van der Stam, J. P. Hofmann, E. Bladt, J. D. Meeldijk, S. Bals and C. de Mello Donega, *Chem. Mater.*, 2018, **30**, 2400–2413.
82 D. C. J. Neo, W. P. Goh, H. H. Lau, J. Shanmugam and Y. F. Chen, *ACS Appl. Nano Mater.*, 2020, **3**, 6489–6496.
83 Y. Kim, H. S. Jang, H. Kim, S. Kim and D. Y. Jeon, *ACS Appl. Mater. Interfaces*, 2017, **9**, 32097–32105.
84 S. H. Park, A. Hong, J.-H. Kim, H. Yang, K. Lee and H. S. Jang, *ACS Appl. Mater. Interfaces*, 2015, **7**, 6764–6771.
85 X. Kang, Y. Yang, L. Huang, Y. Tao, L. Wang and D. Pan, *Green Chem.*, 2015, **17**, 4482–4488.
86 D.-E. Nam, W.-S. Song and H. Yang, *J. Mater. Chem.*, 2011, **21**, 18220–18226.
87 D. P. Singh, T. Vimal, Y. J. Mange, M. C. Varia, T. Nann, K. K. Pandey, R. Manohar and R. Douali, *J. Appl. Phys.*, 2018, **123**, 034101.
88 S. Yamashita, M. Tanabe, T. Araki, M. Shiomi, T. Nishi and Y. Kudo, *J. Phys. Chem. C*, 2022, **126**, 14558–14565.
89 M. Shiraishi, Y. Iso and T. Isobe, *ACS Omega*, 2022, **7**, 33039–33045.
90 R. Terricabres-Polo, T. A. de Bruin, A. Kaul, G. J. H. M. Wilfried and C. d. M. Donega, *Adv. Energy Mater.*, 2024, **14**, 2402375.
91 Y. Chen, F. Ge, Y. Lai, L. Wang, X. Zhao, R. Wang, S. Peng, X.-J. Wu and Y. Zhou, *ACS Appl. Mater. Interfaces*, 2024, **16**, 14072–14081.
92 C. Xia, J. D. Meeldijk, H. C. Gerritsen and C. de Mello Donega, *Chem. Mater.*, 2017, **29**, 4940–4951.
93 W. Lian, D. Tu, P. Hu, X. Song, Z. Gong, T. Chen, J. Song, Z. Chen and X. Chen, *Nano Today*, 2020, **35**, 100943.
94 C. Xia, N. Winckelmans, P. T. Prins, S. Bals, H. C. Gerritsen and C. de Mello Donegá, *J. Am. Chem. Soc.*, 2018, **140**, 5755–5763.
95 J. Wang, H. Ning, J. Wang, S. V. Kershaw, L. Jing and P. Xiao, *ACS Appl. Nano Mater.*, 2022, **5**, 5617–5624.
96 J. Ma, M. Liu, Z. Li and L. Li, *Opt. Mater.*, 2015, **47**, 56–61.
97 R. H. Petrucci, *General Chemistry: Principles and Modern Applications*, Pearson Prentice Hall, 2007.
98 P. B. Mann, K. Afzal, N. J. Long, M. Thanou and M. Green, *RSC Adv.*, 2019, **9**, 16851–16855.
99 C. Pang, S. Hu, C. Guo, J. Wang, S. Zou, Z. Pan, J. Liu, L. Shen, N. Bao, H. Ning, A. Gupta and Z. Gong, *Chem. Mater.*, 2021, **33**, 8775–8785.
100 P. Priyadarshini, S. Senapati, S. Bisoyi, S. Samal and R. Naik, *J. Alloys Compd.*, 2023, **945**, 169222.
101 F. Thiel, C. Palencia and H. Weller, *ACS Nano*, 2023, **17**, 3676–3685.
102 M. S. Pradeepkumar, A. Singh, J. Basu and Md. I. Ahmad, *Ceram. Int.*, 2021, **47**, 32086–32096.
103 M. Goto, K. Sato, S. Yokoyama and H. Takahashi, *J. Mater. Sci.: Mater. Electron.*, 2021, **32**, 9531–9539.
104 E. Dhaene, J. Billet, E. Bennett, I. Van Driessche and J. De Roo, *Nano Lett.*, 2019, **19**, 7411–7417.
105 R. Marin, A. Skripka, Y.-C. Huang, T. A. J. Loh, V. Mazeika, V. Karabanovas, D. H. C. Chua, C.-L. Dong, P. Canton and F. Vetrone, *Chem. Commun.*, 2020, **56**, 3341–3344.
106 V. Perner, T. Rath, F. Pirolt, O. Glatter, K. Wewerka, I. Letofsky-Papst, P. Zach, M. Hobisch, B. Kunert and G. Trimmel, *New J. Chem.*, 2019, **43**, 356–363.
107 M. Kar, R. Agrawal and H. W. Hillhouse, *J. Am. Chem. Soc.*, 2011, **133**, 17239–17247.
108 E. A. Hernández-Pagán, E. H. Robinson, A. D. La Croix and J. E. Macdonald, *Chem. Mater.*, 2019, **31**, 4619–4624.
109 Y. Liu, D. Yao, L. Shen, H. Zhang, X. Zhang and B. Yang, *J. Am. Chem. Soc.*, 2012, **134**, 7207–7210.
110 B. A. Tappan, G. Barim, J. C. Kwok and R. L. Brutchey, *Chem. Mater.*, 2018, **30**, 5704–5713.
111 A. C. Berends, W. van der Stam, Q. A. Akkerman, J. D. Meeldijk, J. van der Lit and C. de Mello Donega, *Chem. Mater.*, 2018, **30**, 3836–3846.
112 E. A. Ho, A. R. Peng and J. E. Macdonald, *Nanoscale*, 2021, **14**, 76–85.
113 S. Koyasu, H. Ikeda and T. Ishigaki, *Langmuir*, 2024, **40**, 18466–18472.

114 F. E. S. Gorris, M. Deffner, S. Priyadarshi, C. Klinke, H. Weller and H. Lange, *Adv. Opt. Mater.*, 2020, **8**, 1901058.
115 J. Choi, W. Choi and D. Y. Jeon, *ACS Appl. Nano Mater.*, 2019, **2**, 5504–5511.
116 D. W. Houck and B. A. Korgel, *Chem. Mater.*, 2018, **30**, 8359–8367.
117 S. Chang, Y. Zhao, J. Tang, Z. Bai, L. Zhao and H. Zhong, *J. Phys. Chem. C*, 2020, **124**, 6554–6561.
118 Y. Zheng, T. J. Slade, L. Hu, X. Y. Tan, Y. Luo, Z.-Z. Luo, J. Xu, Q. Yan and M. G. Kanatzidis, *Chem. Soc. Rev.*, 2021, **50**, 9022–9054.
119 S. Li, H. Shao, K. Ding, M. Yao, M. Dou, Y. Cheng, K. Zhang, N. Yang, Y. Ma and Y. Chen, *ACS Appl. Nano Mater.*, 2023, **6**, 21853–21865.
120 T. Enkhbat, N. Otgontamir and J. Kim, *ACS Appl. Energy Mater.*, 2024, **7**, 1748–1755.
121 N. Al-Salim, A. G. Young, R. D. Tilley, A. J. McQuillan and J. Xia, *Chem. Mater.*, 2007, **19**, 5185–5193.
122 A. Pan, B. He, X. Fan, Z. Liu, J. J. Urban, A. P. Alivisatos, L. He and Y. Liu, *ACS Nano*, 2016, **10**, 7943–7954.
123 K. Nose, H. Fujita, T. Omata, S. Otsuka-Yao-Matsuo, H. Nakamura and H. Maeda, *J. Lumin.*, 2007, **126**, 21–26.
124 D. Ling, M. J. Hackett and T. Hyeon, *Nano Today*, 2014, **9**, 457–477.
125 J.-W. Xiao, S. Ma, S. Yu, C. Zhou, P. Liu, Y. Chen, H. Zhou, Y. Li and Q. Chen, *Nano Energy*, 2018, **46**, 45–53.
126 A. Heuer-Jungemann, N. Feliu, I. Bakaimi, M. Hamaly, A. Alkilany, I. Chakraborty, A. Masood, M. F. Casula, A. Kostopoulou, E. Oh, K. Susumu, M. H. Stewart, I. L. Medintz, E. Stratakis, W. J. Parak and A. G. Kanaras, *Chem. Rev.*, 2019, **119**, 4819–4880.
127 Y. Yin and A. P. Alivisatos, *Nature*, 2005, **437**, 664–670.
128 R. G. Ellis, J. W. Turnley, D. J. Rokke, J. P. Fields, E. H. Alruqobah, S. D. Deshmukh, K. Kisslinger and R. Agrawal, *Chem. Mater.*, 2020, **32**, 5091–5103.
129 D. C. Hayes, S. A. Langdon, R. M. Spilker and R. Agrawal, *ACS Appl. Energy Mater.*, 2024, **7**, 885–895.
130 F. H. Zaki, B. K. Mondal, M. A. H. Pappu, A. T. Abir and J. Hossain, *Phys. Status Solidi A*, 2024, **221**, 2300839.
131 M. Krause, S.-C. Yang, S. Moser, S. Nishiwaki, A. N. Tiwari and R. Carron, *Sol. RRL*, 2023, **7**, 2201122.
132 Y. Jiang, T. Feurer, R. Carron, G. T. Sevilla, T. Moser, S. Pisoni, R. Erni, M. D. Rossell, M. Ochoa, R. Hertwig, A. N. Tiwari and F. Fu, *ACS Nano*, 2020, **14**, 7502–7512.
133 D. Liu, Y. Guo, Y. Yang, J. Liu, X. Yin and W. Que, *J. Alloys Compd.*, 2022, **906**, 164292.
134 J. G. An, H. Tran, D. Kim, S. M. Lee, A. Lee, S. K. Ahn, J.-S. Cho, J. Gwak, T. Kim, I. Jeong and J. H. Park, *Small*, 2024, **20**, 2305796.
135 H. Li, D. Luo, L. Liu, D. Xiong and Y. Peng, *Dalton Trans.*, 2021, **50**, 8837–8844.
136 S. H. Shah and T. Debnath, *J. Phys. Chem. Lett.*, 2024, **15**, 2580–2586.
137 A. Sadhu, T. Salim, Q. Sun, S. Lie, E. Julianto and L. H. Wong, *Adv. Energy Mater.*, 2024, 2403676.
138 H. Liang, J. Feng, C. D. Rodríguez-Gallegos, M. Krause, X. Wang, E. Alvianto, R. Guo, H. Liu, R. K. Kothandaraman, R. Carron, A. N. Tiwari, I. M. Peters, F. Fu and Y. Hou, *Joule*, 2023, **7**, 2859–2872.
139 W. Zhu, Y.-Y. Hu, W. Wang, Y. Xie, W. Xue, F. He and Y. Li, *ACS Appl. Energy Mater.*, 2021, **4**, 5767–5774.
140 D. Zhitomirsky, I. J. Kramer, A. J. Labelle, A. Fischer, R. Debnath, J. Pan, O. M. Bakr and E. H. Sargent, *Nano Lett.*, 2012, **12**, 1007–1012.
141 D. Colombara, H. Elanzeery, N. Nicoara, D. Sharma, M. Claro, T. Schwarz, A. Koprek, M. H. Wolter, M. Melchiorre, M. Sood, N. Valle, O. Bondarchuk, F. Babbe, C. Spindler, O. Cojocaru-Miredin, D. Raabe, P. J. Dale, S. Sadewasser and S. Siebentritt, *Nat. Commun.*, 2020, **11**, 3634.
142 Y. Areerob, C. Hamontree, P. Sricharoen, N. Limchoowong, S. Laksee, W.-C. Oh and K. Pattarith, *RSC Adv.*, 2022, **12**, 15427–15434.
143 H. Song, Y. Lin, Z. Zhang, H. Rao, W. Wang, Y. Fang, Z. Pan and X. Zhong, *J. Am. Chem. Soc.*, 2021, **143**, 4790–4800.
144 S. Rehan, J. Moon, T. G. Kim, J. Gwak, J. Kim, J. W. Kim, W. Jo, S. K. Ahn and S. Ahn, *Nano Energy*, 2018, **48**, 401–412.
145 B. D. Chernomordik, A. R. Marshall, G. F. Pach, J. M. Luther and M. C. Beard, *Chem. Mater.*, 2017, **29**, 189–198.
146 W. J. Daughton and F. L. Givens, *J. Electrochem. Soc.*, 1982, **129**, 173.
147 Z. Zhang, H. Song, W. Wang, H. Rao, Y. Fang, Z. Pan and X. Zhong, *ACS Energy Lett.*, 2022, **8**, 647–656.
148 M. Alemayehu Abate, K. Dehvari, J.-Y. Chang and K. Waki, *Dalton Trans.*, 2019, **48**, 16115–16122.
149 S. Yu, Y. Gong, J. Jiang, S. Wu, W. Yan, X. Li, W. Huang and H. Xin, *Sol. RRL*, 2019, **3**, 1900052.
150 F. He, W. Wang, W. Xue, Y. Xie, Q. Zhou, J. Zhang and Y. Li, *New J. Chem.*, 2020, **44**, 4304–4310.
151 D. Liu, Y. Guo, X. Yin, Y. Yang and W. Que, *Adv. Funct. Mater.*, 2023, **33**, 2210754.
152 Y. Gao, G. Yin and M. Schmid, *Small*, 2023, **19**, 2302581.
153 S. Suresh, D. Abou-Ras, T. H. Chowdhury and A. R. Uhl, *Sol. RRL*, 2023, **7**, 2300437.
154 S.-K. Ming, R. A. Taylor, P. D. McNaughter, D. J. Lewis, M. A. Leontiadou and P. O'Brien, *RSC Adv.*, 2021, **11**, 21351–21358.
155 Y.-M. Liu, R. Niu, S.-A. Li, Y.-J. Feng, H.-B. Ding, J. Zhang, W.-M. Li, Y.-T. Cao, C.-L. Yang, Z. Liu and G.-H. Zhong, *Sol. Energy*, 2024, **271**, 112390.
156 M. Chugh, T. D. Kühne and H. Mirhosseini, *ACS Appl. Mater. Interfaces*, 2019, **11**, 14821–14829.
157 M. Hashemi, Z. Saki, M. Dehghani, F. Tajabadi, S. M. B. Ghorashi and N. Taghavinia, *Sci. Rep.*, 2022, **12**, 14715.
158 M. A. Ruiz-Preciado, F. Gota, P. Fassl, I. M. Hossain, R. Singh, F. Laufer, F. Schackmar, T. Feeney, A. Farag, I. Allegro, H. Hu, S. Gharibzadeh, B. A. Nejand, V. S. Gevaerts, M. Simor, P. J. Bolt and U. W. Paetzold, *ACS Energy Lett.*, 2022, **7**, 2273–2281.
159 Y. H. Jang, J. M. Lee, J. W. Seo, I. Kim and D.-K. Lee, *J. Mater. Chem. A*, 2017, **5**, 19439–19446.

160 Y. Jiang, T. Feurer, R. Carron, G. T. Sevilla, T. Moser, S. Pisoni, R. Erni, M. D. Rossell, M. Ochoa, R. Hertwig, A. N. Tiwari and F. Fu, *ACS Nano*, 2020, **14**, 7502–7512.
161 D. P. Singh, T. Vimal, Y. J. Mange, M. C. Varia, T. Nann, K. K. Pandey, R. Manohar and R. Douali, *J. Appl. Phys.*, 2018, **123**, 034101.
162 T. Rath, D. Scheunemann, R. Canteri, H. Amenitsch, J. Handl, K. Wewerka, G. Kothleitner, S. Leimgruber, A.-C. Knall and S. A. Haque, *J. Mater. Chem. C*, 2019, **7**, 943–952.
163 N. Buatong, I.-M. Tang and W. Pon-On, *Mater. Lett.*, 2017, **199**, 41–45.
164 S. Kim, M. Kang, S. Kim, J.-H. Heo, J. H. Noh, S. H. Im, S. I. Seok and S.-W. Kim, *ACS Nano*, 2013, **7**, 4756–4763.
165 M. D. A. H. Pappu, A. Kuddus, B. K. Mondal, A. T. Abir and J. Hossain, *Opt. Continuum*, 2023, **2**, 942–955.
166 A. Elizabeth, S. K. Sahoo, D. Lockhorn, A. Timmer, N. Aghdassi, H. Zacharias, T. D. Kühne, S. Siebentritt, H. Mirhosseini and H. Mönig, *Phys. Rev. Mater.*, 2020, **4**, 063401.
167 H. Sharma, N. Saini, Lalita, D. Kaushik, A. Kumar and R. Srivastava, *RSC Adv.*, 2024, **14**, 14910–14918.
168 A. S. Cherian, K. B. Jinesh, Y. Kashiwaba, T. Abe, A. K. Balamurugan, S. Dash, A. K. Tyagi, C. Sudha Kartha and K. P. Vijayakumar, *Sol. Energy*, 2012, **86**, 1872–1879.
169 K. Wu, H. Li and V. I. Klimov, *Nat. Photonics*, 2018, **12**, 105–110.
170 Z. Li, X. Zhao, C. Huang and X. Gong, *J. Mater. Chem. C*, 2019, **7**, 12373–12387.
171 R. Sumner, S. Eiselt, T. B. Kilburn, C. Erickson, B. Carlson, D. R. Gamelin, S. McDowall and D. L. Patrick, *J. Phys. Chem. C*, 2017, **121**, 3252–3260.
172 A. R. M. Velarde, E. R. Bartlett, N. S. Makarov, C. Castañeda, A. Jackson, K. Ramasamy, M. R. Bergren and H. McDaniel, *ACS Appl. Energy Mater.*, 2020, **3**, 8159–8163.